1994MNRAS.270..245S

Mon. Not. R. Astron. Soc. **270**, 245–270 (1994)

Gravitational lensing of distant field galaxies by rich clusters – I. Faint galaxy redshift distributions

Ian Smail,* Richard S. Ellis† and Mike J. Fitchett‡
Physics Department, University of Durham, South Road, Durham DH1 3LE

Accepted 1994 April 15. Received 1994 April 8; in original form 1993 December 9

ABSTRACT

From deep optical images of three clusters, selected by virtue of their X-ray luminosity and/or optical richness (1455+22, $z=0.26$; 0016+16, $z=0.55$; 1603+43, $z=0.89$), we construct statistically complete samples of faint field galaxies ($I\leq 25$) that are suitable for probing the effects of gravitational lensing. By selecting clusters across a wide redshift range, we separate the effects of the mean redshift of the faint field population well beyond spectroscopic limits and the distribution of dark matter in the lensing clusters. A significant lensing signature is seen in the two lower redshift clusters, whose X-ray properties are well constrained. Based on these and dynamical data, it is straightforward to rule out field redshift distributions for $I\leq 25$, which have a significant low-redshift excess compared to the no-evolution prediction, such as would be expected if the number counts at faint limits were dominated by low-z dwarf systems. The degree to which we can constrain any high-redshift tail to the no-evolution redshift distribution depends on the distribution of mass in the most distant lensing cluster. In the second paper in this series, we demonstrate that the mass distributions in our lensing clusters are well understood, by reconstructing the full two-dimensional distributions from the lensing signal. The principal result is therefore the absence of a dominant low-z dwarf population to $I\leq 25$.

Key words: galaxies: distances and redshifts – galaxies: evolution – galaxies: formation – galaxies: photometry – cosmology: observations – gravitational lensing.

1 INTRODUCTION

The surface density of faint galaxies is significantly in excess of predictions based on extrapolating to large redshift the known local properties of field galaxies, under the assumption of no evolution (Kron 1978; Peterson et al. 1979; Tyson & Jarvis 1979). The deepest optical counts are inconsistent with both modest and no evolution, irrespective of the cosmological geometry (Tyson 1988; Metcalfe et al. 1990; Yoshii & Takahara 1990; Lilly, Cowie & Gardner 1991), and reveal a gradual bluing with increasing apparent magnitude and no convincing turnover to $B\sim 28$ (Metcalfe et al. 1993).

The high surface density of blue light implies a star formation rate that is sufficient to yield a significant fraction of the metals in disc galaxies today (Cowie 1991). The nature of the population dominating the counts beyond $B\sim 22$ is thus of considerable interest and depends critically on its redshift distribution. To the limits attainable with high-throughput spectrographs on 4-m class telescopes ($B\sim 24$), no significant departure from the predicted no-evolution *shape* of the redshift distribution for B-selected samples has yet been seen (Broadhurst, Ellis & Shanks 1988; Colless et al. 1990, 1993; Cowie, Songaila & Hu 1991; Glazebrook et al. 1994). The most rigorous statement on the redshift distribution can be made to $B=22.5$ (Colless et al. 1993), where the incompleteness in a sizeable sample is less than 5 per cent. At $B\sim 24$ galaxies, where incompleteness remains $\simeq 15$ per cent (Glazebrook et al. 1994), a proportion could be in a high-redshift tail with $z\geq 1$, but it is important to note that the incompleteness is negligible compared to the factor of $\times 4$–6 by which the counts exceed the no-evolution prediction. Notwithstanding the incompleteness, the bulk of the excess population of blue sources, if it exists as a separate entity, must lie within a volume that is consistent with the no-evolution prediction.

*Present address: Caltech 105–24, Pasadena, CA 91125, USA.
†Present address: Institute of Astronomy, Madingley Road, Cambridge CB3 0HA.
‡Present address: Medical School, University of Newcastle, Framlington Place, Newcastle NE2 4HH.

© Royal Astronomical Society • Provided by the NASA Astrophysics Data System

1994MNRAS.270..245S

Determining the nature of the excess population is hard, because of the difficulty of identifying representative examples for scrutiny. So long as the excess population is statistically defined, physical properties such as luminosity functions or clustering scalelengths cannot be reliably determined. Following Broadhurst et al.'s (1988) suggestion that the excess is associated with galaxies with intense [O II] spectral emission, Cole et al. (1993) found the excess population to be cospatial with its quiescent counterpart, and Colless et al. (1994) found that such sources are often double systems. Such observations are *consistent* with the idea (but by no means prove it) that star formation induced by merging may simultaneously explain the counts and redshift data (cf. Broadhurst, Ellis & Glazebrook 1992). On the other hand, Efstathiou et al. (1991) and subsequent workers (e.g. Couch, Jurcevic & Boyle 1993) present convincing evidence for a marked decrease in the angular clustering of $B \simeq 26$ galaxies, which may support an alternative viewpoint, which is that the blue light arises in recent star formation in a separate dwarf galaxy population whose present-day counterparts cannot be found (cf. Babul & Rees 1992). Some support for this model has come from limited spectroscopic surveys, which have concluded that there is an excess of dwarf systems at the required redshifts (Cowie et al. 1991; Tresse et al. 1993).

The importance of the angular correlation function studies of faint field samples lies in the fact that virtually *all* of the sources at $B=26$ represent the excess population, i.e. difficulties in identifying the excess populations are largely removed. If it were possible to determine redshifts and luminosities for such a faint sample, even if only statistically, significant progress could be made. If the counts were dominated to the faintest limits by a recent era of dwarf galaxy formation, as proposed by Babul & Rees, it is conceivable that the median redshift would hardly change for samples fainter than $B \simeq 24$. For a simple merger model, the median redshift closely tracks the no-evolution prediction (cf. Broadhurst et al. 1992), whereas, if a significant fraction of $B=26$ galaxies originates in a primordial population, there would be a rapid increase in the median redshift.

Unfortunately, conventional optical spectroscopy is rapidly approaching a hard faintness limit for two reasons. State of the art faint object spectrographs, such as LDSS-2 (Allington-Smith et al. 1994) and MOSIS (Le Fèvre 1993), secure redshifts to $B=24$ in 4–6 h exposures. Even with 10-m class telescopes, it will be painful to push the limits much beyond $B=25$. More importantly, Glazebrook et al. (1994) demonstrate convincingly how, as [O II] 3727 Å is redshifted beyond 8000 Å (for sources with $z>1$), no useful diagnostic features can be seen in the optical region, resulting in severe redshift incompleteness in any $z>1$ tail. What is needed, therefore, is an independent method for determining the mean cosmological distance to a sample that is substantially fainter than $B=24$.

In this paper, we describe how the gravitational lensing signal produced by rich clusters at different distances can constrain the redshift distribution of the faint galaxy population. The relevant samples are chosen to have $I \leq 25$ (corresponding approximately to $B \lesssim 27$). The technique is based on the weak distortion of background field galaxies first explored in a pioneering paper by Tyson, Valdes & Wenk (1990). We have, however, extended the method, not only by imaging the field population to the same depth through several clusters at different distances, but also, significantly, by verifying the relative distribution of dark matter in the lensing clusters, using a new inversion technique developed by Kaiser & Squires (1992). The latter result forms the basis of the second paper in this series (Smail et al. 1994, Paper II), which should, ideally, be read in conjunction with this paper.

A plan of this paper follows. In Section 2, we briefly review the lensing test proposed. This serves to explain in more detail the logic of this paper and its companion article. In Section 3, we discuss the new observations, including target selection, data acquisition and reduction. Section 4 presents various statistical tests we have applied to the faint catalogues in the context of model redshift distributions. Our constraints are discussed in Section 5 and our conclusions are presented in Section 6.

2 THE LENSING METHOD AND PREVIOUS WORK

Our method to determine the mean distance to an $I \leq 25$ sample works as follows. The gravitational lensing of background galaxies by the cluster potential produces a coherent pattern of image distortions, orthogonal to the cluster radius vector (Grossman & Narayan 1988). Although the weak signal is superimposed upon intrinsic ellipticities and orientations of the population, its coherent nature can be used to overcome the low signal-to-noise ratio inherent in the statistics of faint image shapes. Of course, neither faint cluster members nor sources foreground to the cluster contribute to the lensing signal.

The most elementary test measures the proportion of objects, to a fixed apparent magnitude limit, aligned tangentially to the radius vector to the lens centre. In the idealized case of a sample of identical lenses at different redshifts $z^i_{\rm lens}$, $i=1 \ldots n$, the variation in the fraction of aligned images with redshift delineates the shape of the field galaxy redshift distribution $N(z)$. In practice, of course, clusters have a variety of lensing powers, and the observed fraction is controlled not only by the combination of the field, $N(z)$ and $z_{\rm lens}$, but also by the amount and concentration of mass in the lens, $M(r)$. To decouple these two factors, more complex analyses are required.

The first stage of complexity is to allow some freedom in the core radius $r_{\rm c}$ (kpc) and the depth of the gravitational potential well [parametrized by $\sigma_{\rm cl}$ (km s^{-1}), the velocity dispersion of the cluster] in a given cluster, according to a simple isothermal model. These parameters can be constrained, to some extent, from X-ray imaging data and galaxy dynamics. By applying a joint likelihood technique across all three clusters, each of which has been imaged in the same conditions, we can test whether the lensing signals are consistent with a sequence of 'test' field redshift distributions $N(z)$.

It may be, however, that the distribution of dark matter in a cluster bears little relation to that observed for the X-ray gas and cluster members. In such a situation, the test described above would give misleading results. The companion paper to this article shows how the lensing signal measured *across* the cluster can be inverted, using a new technique developed by Kaiser & Squires (1992), to define a projected 2D map of the lensing mass at a resolution that is adequate to check its concentration. Although the technique

© Royal Astronomical Society • Provided by the NASA Astrophysics Data System

1994MNRAS.270..245S

does not yield an *absolute* estimate of the total cluster mass, the results show how closely the dark and baryonic matter are distributed. This important result is essential to remove the ambiguities in the determination of the median redshift for an $I \leq 25$ field sample.

Our method is qualitatively different from previous lensing probes of the faint galaxy distribution, and thus we briefly review those studies in the context of our paper. Tyson et al. (1990) presented a pioneering analysis of two X-ray-luminous clusters: Abell 1689 ($z=0.18$, $L_X = 1.7 \times 10^{45}$ erg s^{-1}, $\sigma_{cl} = 1800 \pm 200$ km s^{-1} and Cl1409+52 ($z=0.46$, $L_X = 9.2 \times 10^{44}$ erg s^{-1}, $\sigma_{cl} \sim 3000$ km s^{-1}). The small CCD format available at the time restricted imaging to radii $r \leq 380$ and 500 kpc, respectively (we adopt $H_0 = 50$ km s^{-1} Mpc^{-1} and $q_0 = 0.5$ throughout). Samples were selected with $B \in [22, 26]$ equivalent to $I \in [20, 24]$, but only the bluer galaxies showed alignment tangential to the cluster centres. The excess aligned component is relatively small, however, amounting to $\simeq 30$–40 galaxies in A1689 and only 12 in Cl1409+52. Using this signal, Tyson et al. claimed that at least 70 per cent of the $B \in [22, 26]$ population has $z \geq 0.9$. Applying a statistic based on the alignment signal, they also derived radial 'mass' profiles for the clusters, but it transpires that these profiles represent the surface potential (cf. Kaiser & Squires 1992).

Our study extends the analysis of Tyson et al. (1990), by constructing a more extensive sample of faint galaxies with large format CCD detectors and applying a variety of new analytic techniques. There are also some important strategic differences. First, by selecting in B and restricting the cluster redshifts to $z \leq 0.5$, Tyson et al. would not be sensitive to a genuinely high-redshift population whose Lyman limit would have shifted beyond the observing passband. By selecting in a near-infrared passband and using long baseline colours, we can rectify this and more easily remove contaminating cluster members. The second important difference is increased depth. By probing a magnitude deeper in good seeing, we reach a surface density of sources that is sufficiently high to allow recovery of possible substructure in the cluster mass distribution, using the Kaiser & Squires inversion technique. Simulations show that this would not be possible at Tyson et al.'s brighter limit.

Very recently, Kneib et al. (1994) have utilized a rather different method to constrain the redshift distribution of $B \simeq 27$ galaxies. They select a single cluster, Abell 370 ($z=0.37$), whose mass profile is well constrained from arcs of known redshift (Soucail et al. 1988). They visually identify a candidate list of likely arclets and attempt to 'invert' the lens equations to derive their cosmic distances *individually*. Whilst the individual arclet redshifts may be correct, however, by using a single cluster, an unbiased $N(z)$ that is appropriate for a $B \leq 27$ sample cannot be simply constructed.

3 THE DATA

3.1 Observational considerations

The lensing signal we seek is intrinsically very weak and could easily be affected by systematic errors. To account for such errors, we have simulated images of clusters, taking into account all likely observational effects. These simulations, discussed below, are used to calibrate the statistics that apply to the real data sets. Foremost is the need to measure ellipticities of faint galaxies over a wide field. The typical scale size of an $I \simeq 25$ galaxy is 0.3–0.7 arcsec, thus subarcsecond seeing in the selection passband is critical. In addition, the pixel scale must sample the seeing disc appropriately, in order to eliminate pixellation effects in the ellipticity measurements (pixels $\lesssim 0.3$ arcsec). With a large format EEV CCD, the $f/4$ TAURUSII imaging Fabry–Perot system on the 4.2-m William Herschel Telescope (WHT) has 0.27-arcsec sampling of a 5×5 arcmin^2 field, making it ideally suited to this project.

The two passbands (V and I) were selected to provide a colour baseline consistent with the sensitivity of the available large format EEV CCD. To reach a surface density of 40 arcmin^{-2} in the I band requires a completeness limit of $I=25$ (Lilly et al. 1991). Data in V permit the discrimination of cluster members as well as exploration of a possible variation of the lensing signal with colour. Typically, $V-I \sim 1.5$, leading to a V completeness limit of $V=26.5$.

Excellent seeing is only needed for the I detections, which are then used to provide statistical estimates of shapes and orientations on a galaxy-by-galaxy basis. Within the galaxy image, we estimated a minimum signal-to-noise ratio per pixel of $\simeq 2.5$, corresponding to $50\,\sigma$ over a 1.5-arcsec FWHM. To achieve this signal-to-noise ratio at the chosen completeness limit required on-source integrations of 20 ks in I and 10 ks in V per cluster.

Most published moderate- and high-z cluster catalogues were identified, either from peaks in the projected surface density of optical galaxies (Abell, Corwin & Olowin 1989; Gunn, Hoessel & Oke 1989; Couch et al. 1991) or from deep X-ray observations (Henry et al. 1992). Although the negative evolution claimed for the number density of luminous X-ray clusters at relatively low redshifts (Edge et al. 1990) seems in conflict with the abundance of high-redshift optical clusters (Couch et al. 1991), we conclude that X-ray observations will provide us with a tracer of the most massive systems at a given epoch and should be less sensitive to projection effects. Accordingly, we chose three clusters (1455+22, $z=0.26$; 0016+16, $z=0.55$; 1603+43, $z=0.89$), primarily on the basis of their X-ray luminosities. Further details of the clusters are provided in later sections (see also Table 1).

Observations were made in two runs, in 1990 July and 1991 May, on the WHT; the journal is presented in Table 2.

Table 1. Details of the three clusters observed.

Cluster	z	R.A. (1950)	Dec. (1950)	L_X	σ_{cl}	Scale (kpc/arcsec)
Cl1455+22	0.259	$14^h55^m00^s.6$	22°32′20″.7	1.60 10^{45}	~ 700	5.0
Cl0016+16	0.546	$00^h15^m56^s.0$	16°09′36″.0	1.43 10^{45}	1324	7.4
Cl1603+43	0.895	$16^h02^m45^s.0$	43°12′54″.0	1.1 10^{44}	—	8.4

© Royal Astronomical Society • Provided by the NASA Astrophysics Data System

1994MNRAS.270..245S

Table 2. Journal of observations for two runs made on the William Herschel Telescope (WHT), in 1990 July and 1991 May.

WHT Run #1 Observing Log

Cluster	Filter	R.A. (1950)	Dec. (1950)	Date	Seeing	Exposure (s)
Cl0016+16	*V*	$00^h15^m56^s.0$	$16°09'36''.0$	21/22 July 1990	1".05	11000
Cl0016+16	*I*	$00^h15^m56^s.0$	$16°09'36''.0$	22/23-24/25 July 1990	0".95	25500
Cl1603+43	*V*	$16^h02^m45^s.0$	$43°12'54''.0$	21/22 July 1990	1".00	9000
Cl1603+43	*I*	$16^h02^m45^s.0$	$43°12'54''.0$	22/23-24/25 July 1990	0".90	20500

Telescope: 4.2m WHT
Instrument: TAURUSII f/4
Detector: GEC EEV (880 × 1180 pixels)
Pixel size: 0".27 /pixel

WHT Run #2 Observing Log

Cluster	Filter	R.A. (1950)	Dec. (1950)	Date	Seeing	Exposure (s)
Cl1455+22	*V*	$14^h55^m00^s.6$	$22°32'20''.7$	11/12-12/13 May 1991	1".00	12000
Cl1455+22	*I*	$14^h55^m00^s.6$	$22°32'20''.7$	11/12-12/13 May 1991	0".90	20850
Cl1603+43	*V*	$16^h02^m45^s.0$	$43°12'54''.0$	13/14 May 1991	1".5	11500
Cl1603+43	*I*	$16^h02^m45^s.0$	$43°12'54''.0$	12/13 May 1991	0".85	4800

Telescope: 4.2m WHT
Instrument: TAURUSII f/4
Detector: GEC EEV (1280 × 1180 pixels)
Pixel size: 0".27 /pixel

During the first run, we encountered photometric conditions with very good seeing. During the second portion of the second run, however, the seeing deteriorated beyond the limit we considered suitable for this study (1.0-arcsec FWHM). Accordingly, the data taken during this period were only used for photometric work and were not used to analyse image shapes for the lensing analysis.

The observations comprised multiple $\lesssim 1000$-s exposures of two target clusters in a single passband each night. The exposures were 'dithered' on a rectangular grid with 10–15 arcsec spacing and, by combining data for both clusters, a sky flatfield for the entire night was constructed and used to process the images. Numerous shorter exposures of standard stars were also taken at regular intervals throughout the night, in order to track variations in the transparency. Further twilight flatfields were taken each night. The transparency was very stable, with photometric zero-point errors on the final frames of below 0.01 mag.

The reduction of in-field dithered images is a more complex affair than normal image reduction, especially for a rich cluster containing many bright large galaxies. The reduction was performed using IRAF and consisted of the following steps.

(i) After bias subtraction and trimming, large-scale gradients across the images were removed using the twilight flats.

(ii) An object detection algorithm (FOCAS, Valdes 1982) was then used to replace all pixels contained within bright objects with random sky values drawn from surrounding regions.

(iii) The cleaned frames were then median-combined to give 'superflats', which contain both the pixel-to-pixel sensitivity variations and residual large-scale variations arising from the mismatch of the twilight flatfield and the actual flatfield.

(iv) The pre-cleaned images were then flatfielded using the superflats to produce the final reduced images.

A comparison of offset frames of the same field after alignment revealed an uncorrected radial distortion in the positions of all sources. Investigations revealed this to be an inherent feature of the focal reducing optics. Uncorrected, this would produce a serious reduction in the off-axis image quality. To remove this distortion, every image was geometrically remapped according to a system of fiducial references, defined by a large number ($\gtrsim 100$) of objects distributed over the frame. A spline surface was fitted to the $\boldsymbol{X}$ and $\boldsymbol{Y}$ distortion vectors and each pixel was remapped according to linear interpolation within this surface. The remapping successfully removed the distortion to a level below 0.07 arcsec over the entire frame. The remaining residuals appear random and thus should add incoherently when the frames are stacked, resulting in an uncorrelated rms error in the ellipticity of a typical faint object of ≤ 0.5 per cent.

The processed frames were then combined using a broad median algorithm with an additive scaling offset to account for variations in sky brightness. This provided two final frames, one in each passband, for each of the three clusters. The typical $1\,\sigma$ surface brightness limit in the two bands are: $\mu_V = 28.9$ mag arcsec^{-2} and $\mu_I = 27.8$ mag arcsec^{-2}. We now discuss the creation of reliable objects catalogues from these deep images.

3.2 Object selection

The size and depth of the frames obtained are such that, when optimizing the analysis technique, it is most efficient to

© Royal Astronomical Society • Provided by the NASA Astrophysics Data System

1994MNRAS.270..245S

run tests on small, but representative, 1×1 arcmin^2 regions (Fig. 1). The FOCAS object detection algorithm is described in detail by Jarvis & Tyson (1981) (see also Valdes 1982). The two main parameters that control the detection characteristics of the algorithm are the threshold cut (in units of the global sky sigma, $\sigma_{\rm sky}$) and the minimum object area (in pixels). These parameters were optimized by visually checking the success rate of faint object detections against obvious spurious sources. The optimum combination was a threshold of 2.5 $\sigma_{\rm sky}$ per pixel over an area of 10 pixels, which corresponds roughly to a 25 $\sigma_{\rm sky}$ detection within the seeing disc.

Object detection is performed on co-added $V+I$ images, combined such that, in the final image, a flat spectrum source ($f_\nu \simeq$ constant – representative of the faintest objects) has equal flux contributions from each filter. Tests show that this approach both provides a fainter detection limit for images and improves detection of objects with very extreme colours. These frames are reproduced in Figs 2(a)–(c). After initial detection on the $V+I$ image, the object areas were evaluated and analysed on the individual V and I frames. These catalogues were merged to define a final list of sources detected on both frames. Any objects whose isophotes touch the frame boundaries, and thus have ill-defined shapes, were rejected at this point.

To determine the effective completeness limit for object detection in the individual bands, we created a high signal-to-noise faint galaxy, by median-combining a large number of faint galaxy images from the data. This was then scaled and repeatedly added into a region of the cluster frame. The

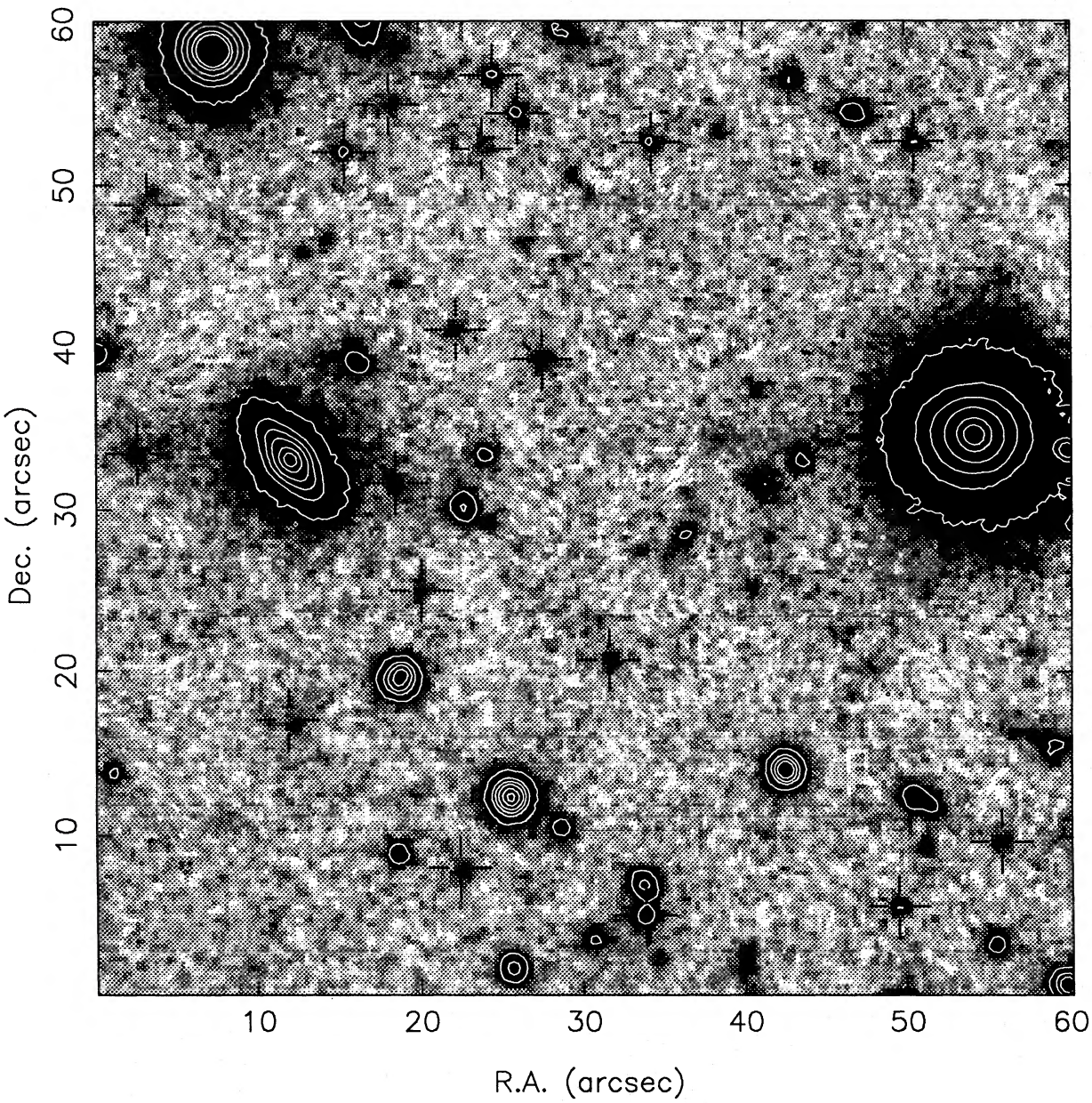

Figure 1. A 1×1 arcmin^2 test area in the 1455 + 22 frame. This is a 20.8-ks I exposure, with 40 objects detected above $I = 25$. Those objects in the faintest analysis sample ($I_{\rm iso} \in 24$–25) are marked.

© Royal Astronomical Society • Provided by the NASA Astrophysics Data System

1994MNRAS.270..245S

detection process was then rerun, and the success of detection of the images, as a function of magnitude, gave the completeness limit for the catalogue for that band. As noted earlier, we actually selected from the combined $V+I$ image, which means that the limits from the completeness simulations are, in fact, lower bounds on the actual completeness of our catalogues. We adopted a fixed I magnitude limit in all three catalogues, so that a well-defined redshift distribution could be compared across all clusters.

Standard aperture photometry in a 3-arcsec aperture was then performed on all the objects, using seeing-matched images, and aperture colours calculated. The resulting parameters for each object are its position, intensity-weighted second moments calculated from the better-seeing I image, isophotal I magnitude and $V-I$ aperture colour. The colour magnitude data for each cluster are shown in Figs 3(a)–(c). The 80 and 50 per cent completeness limits for the individual catalogues are marked on these figures. We now discuss the individual clusters and their associated faint object catalogues.

3.3 The lensing clusters

3.3.1 1455+22 (z=0.26)

This cluster (Fig. 2a) was discovered as a serendipitous source in the *Einstein* Medium Sensitivity Survey (Henry et al. 1992). On the basis of broad-band galaxy photometry, it was initially suspected to be a $z=0.7$ cluster (Schild et al. 1980), but subsequent spectroscopy confirmed a lower redshift (Mason et al. 1981). Unfortunately, redshifts are only available for four members, including the dominant central galaxy ($z=0.258$). Although the formal velocity dispersion is only ~ 700 km s^{-1}, with only four velocities it would be

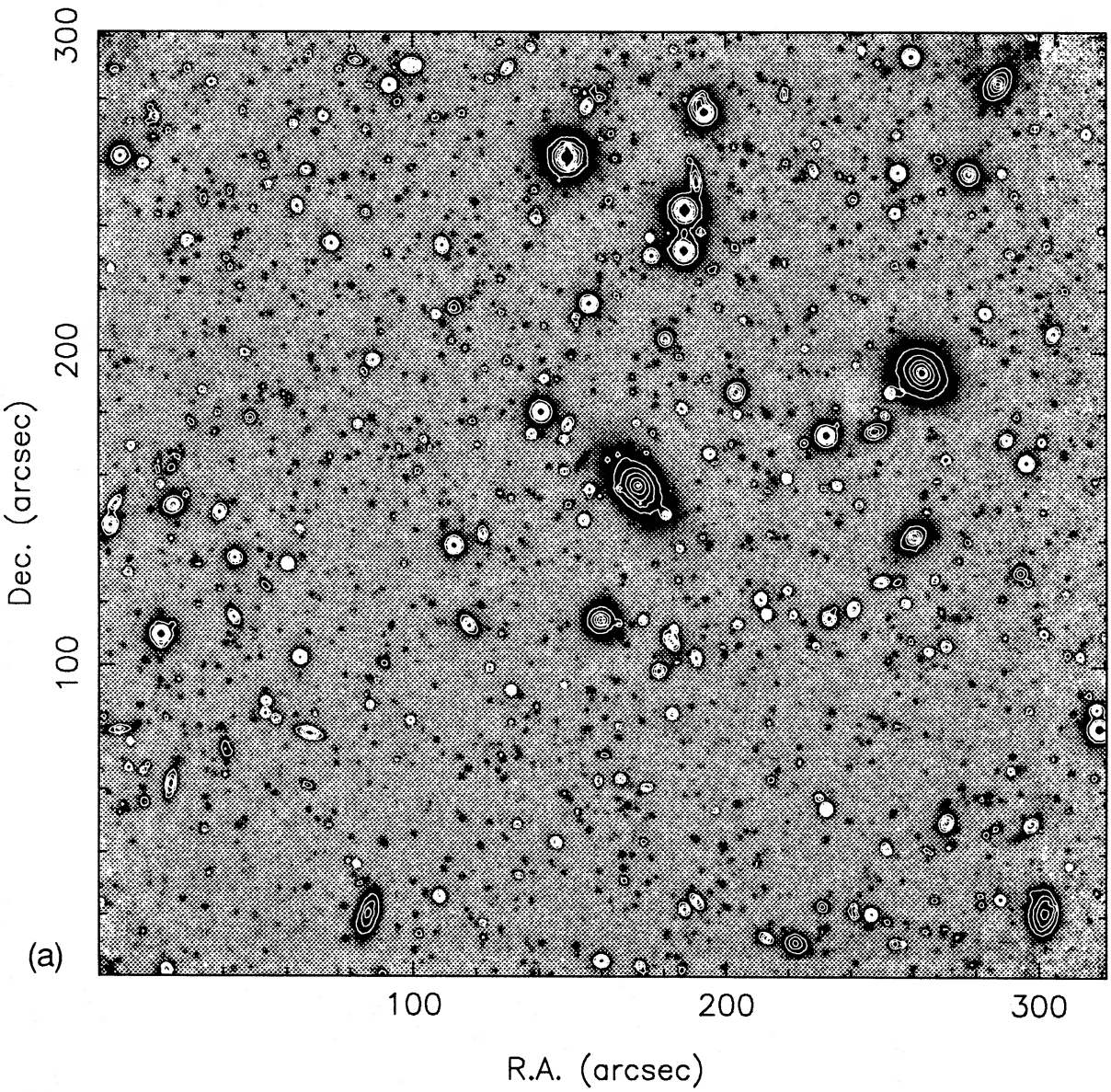

Figure 2. Composite $V+I$ images of the clusters: (a) 1455+22 ($z=0.26$), (b) 0016+16 ($z=0.55$), and (c) 1603+43 ($z=0.89$). The total exposure times are 33.0, 36.5 and 45.8 ks, respectively, and the scales are in arcsec, with east to the left and north at the top.

© Royal Astronomical Society • Provided by the NASA Astrophysics Data System

1994MNRAS.270..245S

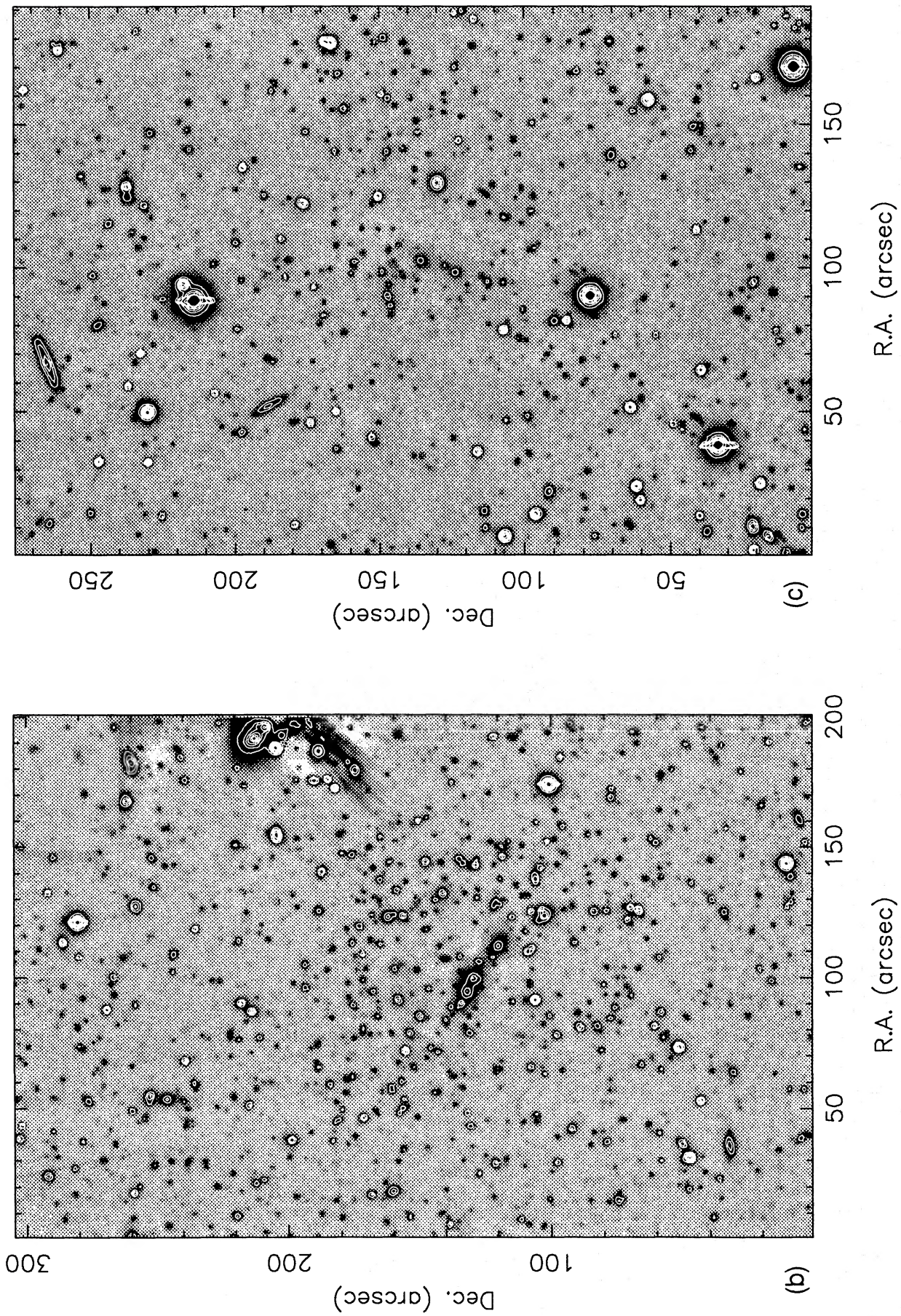

Figure 2 – *continued*

© Royal Astronomical Society • Provided by the NASA Astrophysics Data System

1994MNRAS.270..245S

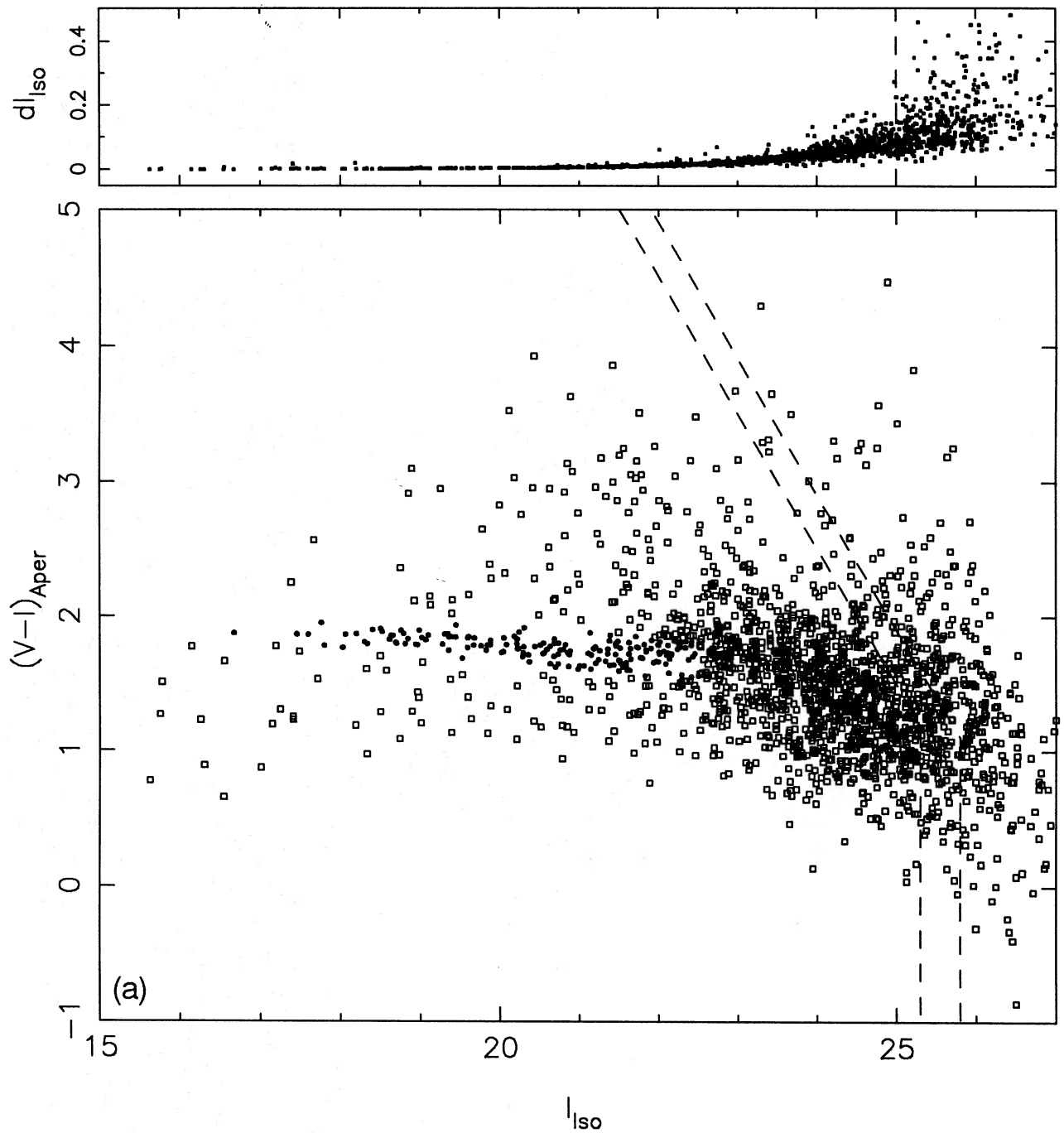

Figure 3. The $V-I$ colour–magnitude diagrams for the clusters (a) 1455 + 22, (b) 0016 + 16, and (c) 1603 + 43. Galaxies with colours similar to an E/S0 at the cluster redshift are shown (●), as well as the 80 and 50 per cent completeness limits for the various catalogues, calculated from simulations. Also shown are the photometric errors as a function of magnitude for the entire samples; the line marked is the chosen magnitude limit for the total sample $I = 25$.

possible for the observations to be consistent with an intrinsic dispersion of 1500 km s^{-1} for 40 per cent of the time. In contrast, it is one of the most X-ray-luminous clusters known: $L_X \sim 1.598 \times 10^{45}$ erg s^{-1} in the 0.3–3.5 keV band. The target has been imaged in deep pointed observations with *ROSAT* High Resolution Imager, in parallel with our gravitational lensing study, and this image is presented in the companion paper.

Examining the colour–magnitude diagram for this field (Fig. 3a), it is straightforward to locate a well-defined cluster colour–magnitude relation (which extends over 6 mag to $I = 22.0$) at the appropriate colour for a population of early-type members at this redshift. (It should be noted that all five objects originally thought by Schild et al. to be at $z = 0.7$ lie on this relation.) By comparing object densities on the colour–magnitude plane with those, suitably scaled, for the

© Royal Astronomical Society • Provided by the NASA Astrophysics Data System

1994MNRAS.270..245S

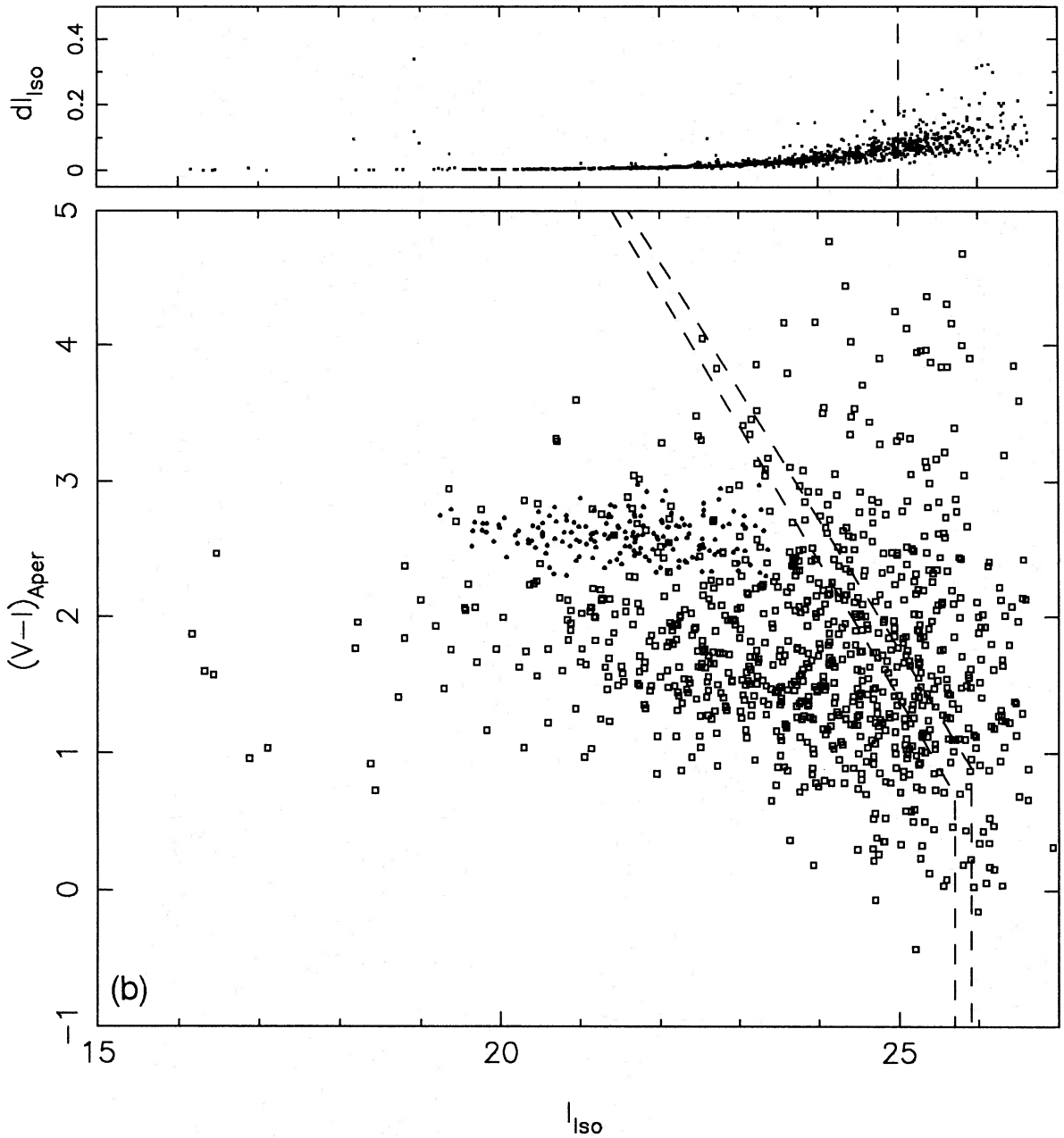

Figure 3 – *continued*

other clusters, no statistical excess representing the cluster was found either beyond $I=22.0$ or bluer than the colour–magnitude relation. The tightness of the relation over this range $[\Delta(V-I)=0.04$ mag$]$ verifies the excellent photometric precision achieved. Using the test discussed in Section 3.2, the 80 per cent photometric completeness limits were found to be $I=25.3$ and $V=26.5$. An $I=25$ galaxy corresponds to a 17 σ detection within the seeing disc.

We define our 'field' sample to be those sources whose colours lie off the narrow colour–magnitude sequence of the cluster (marked as open circles on Figs 3a–c). This is a fair approximation, given the limits on a blue excess from the object densities on the colour–magnitude plane and the observation that, even in the strongest 'Butcher–Oemler' clusters, the fraction of cluster galaxies lying outside this narrow colour–magnitude sequence is typically less than 30 per cent (cf. Oemler 1992). Two simple checks have been made on this procedure: in Fig. 4 the number counts derived are compared with those of genuine 'blank fields' (Lilly et al. 1991), finding good agreement, and we have also examined the radial distribution of our 'field' objects, and this reveals no centrally clustered component.

The above procedure yields 180 early-type members that are brighter than $I=22$ over the 5×5 arcmin^2 field. Only 17 galaxies in the inner 500 kpc lie within the range $[m_3, m_3+2]$, compared to 48 for the Coma cluster (Metcalfe 1983). Clearly, $1455+22$ is only one-third as optically rich as Coma, a result that is consistent with the poorly

© Royal Astronomical Society • Provided by the NASA Astrophysics Data System

1994MNRAS.270..245S

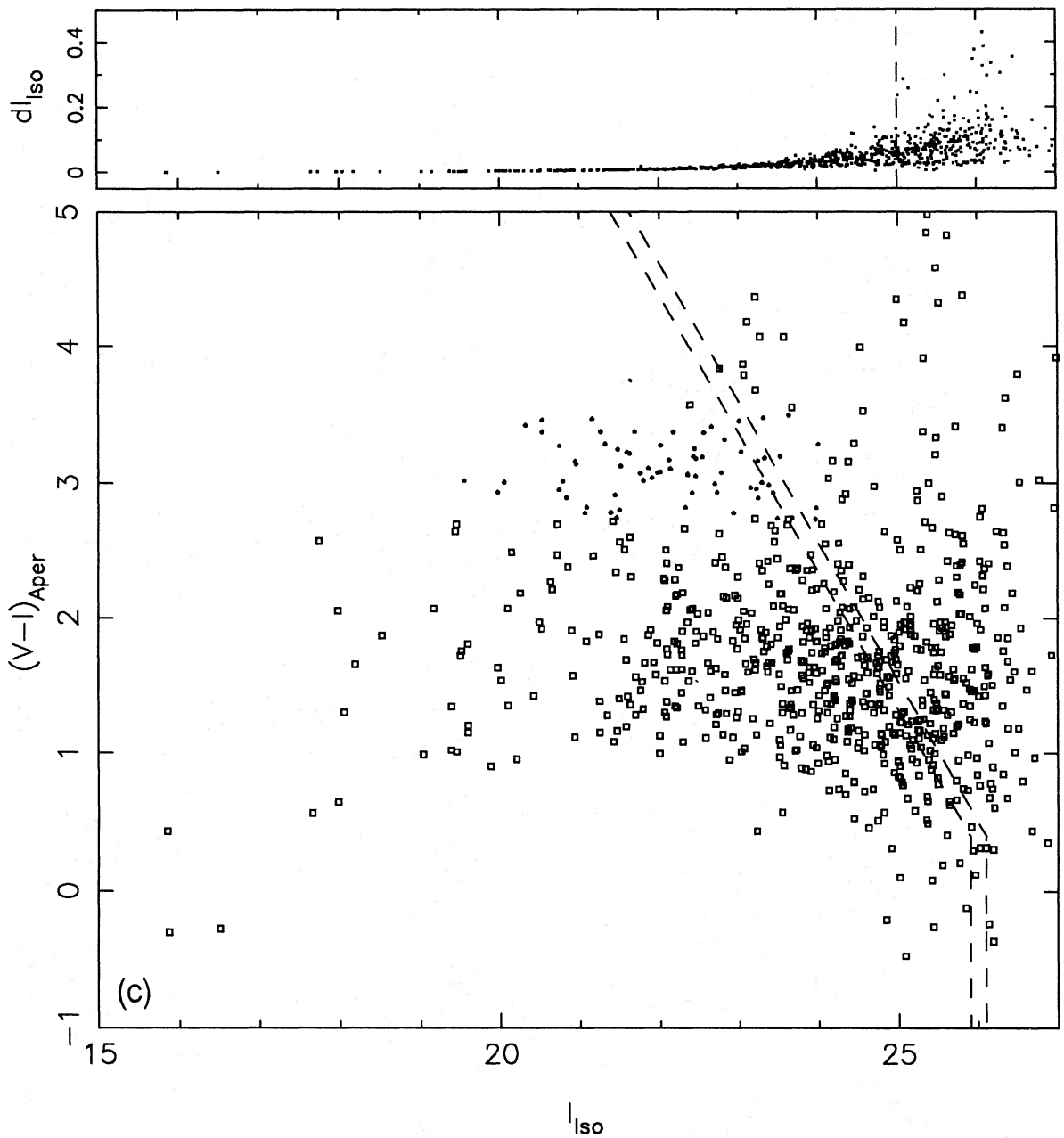

Figure 3 – *continued*

determined velocity dispersion. On the other hand, the extremely high X-ray luminosity and the presence of a large cD galaxy both point to a deep and centrally concentrated cluster potential.

3.3.2 0016+16 (z = 0.55)

This cluster was discovered by Richard Kron on a 4-m Mayall prime focus IIIa-F plate (Spinrad 1980). The redshift is $z = 0.545$ (Dressler & Gunn 1992) and the rest-frame velocity dispersion derived from 30 members is $\sigma_{cl} = 1324$ km s^{-1}. The cluster has been the subject of several photometric studies because of Koo's (1981) original claim that, despite the high redshift, there is little or no population of associated blue members. The large population of intrinsically red galaxies has been studied by Ellis et al. (1985) and Aragón-Salamanca et al. (1993). The cluster was the subject of one of the deepest *Einstein* High Resolution Imager exposures (White et al. 1981) and has been recently imaged with the PSPC on board *ROSAT*.

The cluster has no dominant central galaxy. The core contains three bright galaxies in a linear structure (Fig. 2b) and the peak in the galaxy surface density lies slightly to the south-west of this structure. The central members define an elliptical form (axial ratio ~0.6) and a core radius of ≃330 kpc. The optical counts indicate a richness twice that of Coma, but Ellis et al. indicate this may be an overestimate, because of contamination by a foreground system at $z \sim 0.3$.

© Royal Astronomical Society • Provided by the NASA Astrophysics Data System

1994MNRAS.270..245S

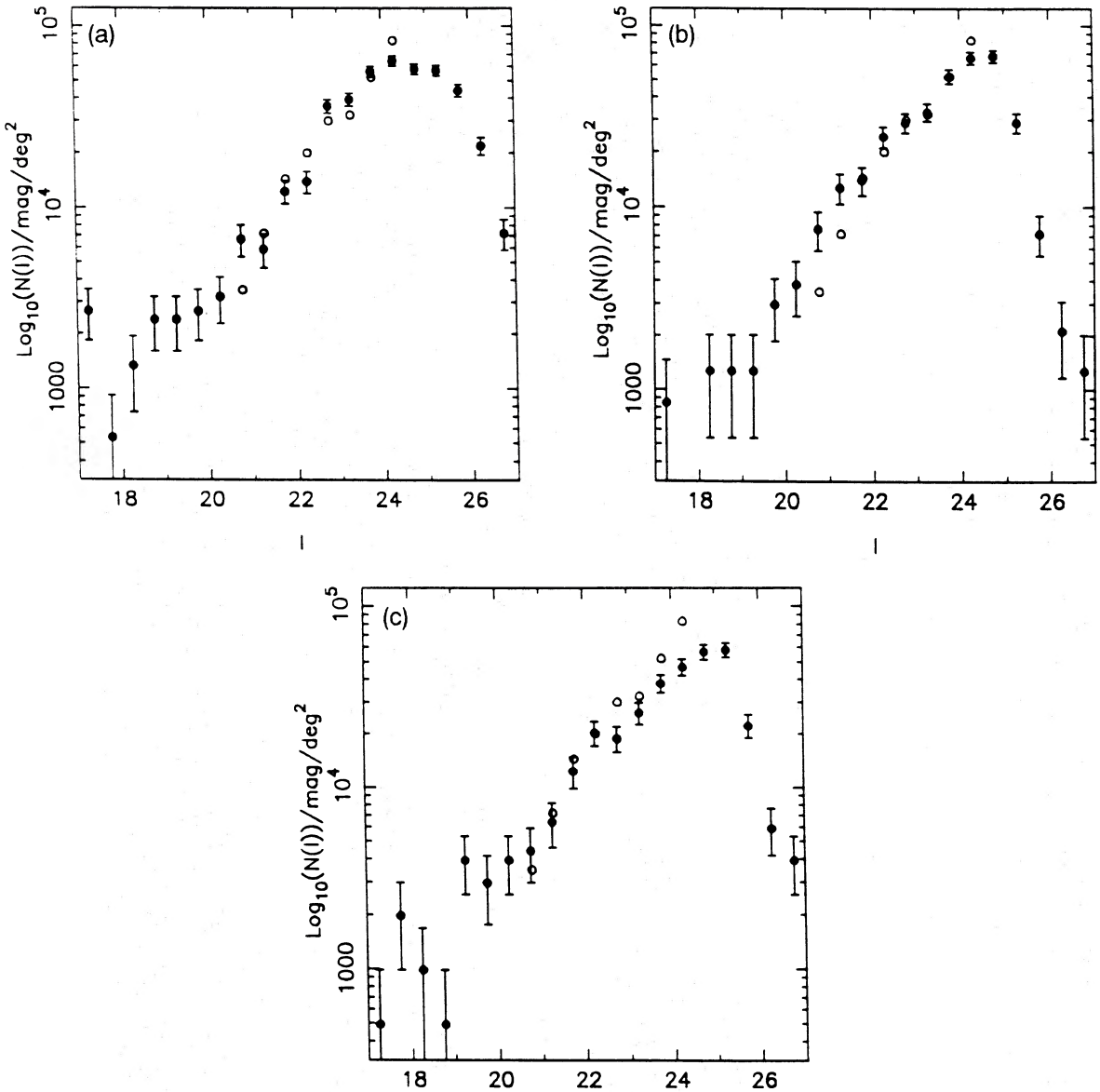

Figure 4. Differential number counts in I of (a) 1455+22, (b) 0016+16, and (c) 1603+43, after removal of the cluster members (●), compared to the Lilly et al. (1991) field counts (○). The deficit of field galaxies in the more distant clusters, at faint magnitudes, arises from the cluster selection criteria.

The cluster was detected in the deep *Einstein* HRI exposure with $L_X \simeq 1.43 \times 10^{45}$ erg s^{-1} in the 0.5–4.5 keV band. The best-fitting isothermal β-model has an X-ray core radius of 220 kpc (White et al. 1981), although a strong cooling flow would affect this result. Although the published X-ray map has only a 30-arcsec (220 kpc) resolution, it also shows a roughly elliptical structure around the optical centre, which is similarly orientated. Finally, the cluster has a detectable Sunyaev–Zel'dovich decrement (Birkinshaw et al. 1994). In summary, therefore, the cluster appears to be very rich and centrally concentrated, and ideally suited for lensing studies.

Following the methods discussed for 1455+22, the 80 per cent completeness limits in this case are $V=26.4$ and $I=25.7$, and the $I=25$ limit corresponds to a 19 σ detection in the seeing disc. Using the colour–magnitude sequence, the cluster can be detected down to $I=23.5$. Additional colour information is available from a deep 6-ks R-band service exposure taken with a large format EEV CCD at the 2.5-m INT prime focus. This is adequate to provide colours, to $I=24$, to better than 0.2 mag. It was therefore possible to double-check the colours of cluster members on a $(V-R)$–$(R-I)$ plane. The final cluster sample contains 174 galaxies to $I=23.5$, of which 83 lie in the interval $[m_3, m_3+2]$. Significantly, the colour-selected members delineate a complex 2D structure. The main feature is a partial annulus consisting of four separate clumps surrounding the cluster centre on the west.

The colour distributions shown in Fig. 5 demonstrate that, whilst we have successfully removed the bulk of the cluster members, the foreground groups identified by Ellis et al. (1985) are apparent as an excess of objects brighter than

© Royal Astronomical Society • Provided by the NASA Astrophysics Data System

1994MNRAS.270..245S

$I=22$ in the I-counts. Removal of this source of further contamination is not possible with the existing data sets.

Again, the scatter about the cluster colour–magnitude relation is surprisingly small [$\Delta(V-I)=0.06$ mag]. Since, at $z=0.55$, $V-I$ is equivalent to the rest-frame $U-V$, we can directly compare this value with the intrinsic dispersion seen in Coma [$\Delta(U-V)\leq 0.04$ mag] by Bower, Lucey & Ellis (1992). At a look-back time of 6 Gyr, there appears to be no evidence for a large increase in this dispersion. If 0016 + 16 is a representative cluster, then, within the framework

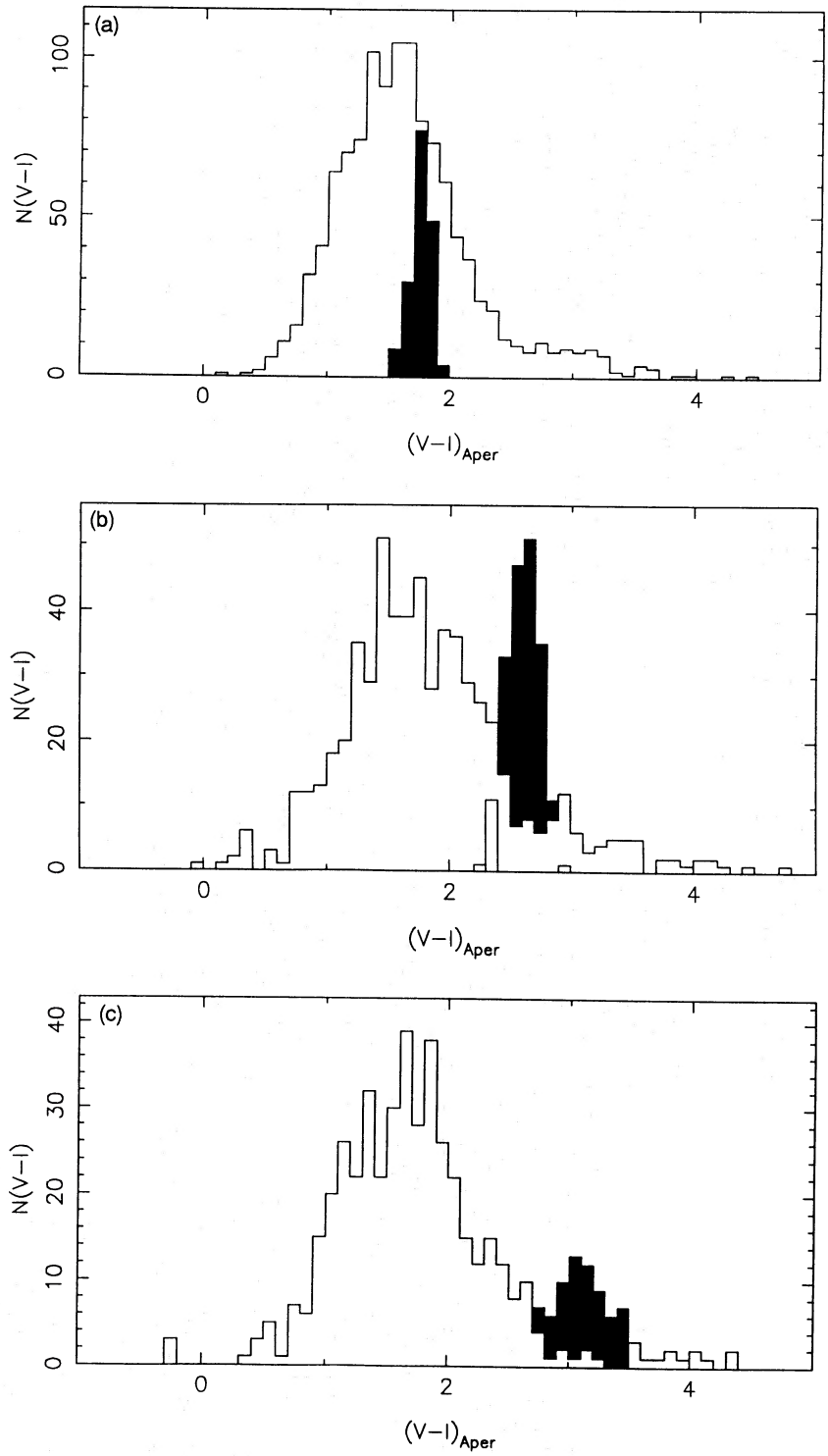

Figure 5. $V-I$ colour distributions for the clusters (filled) and field galaxies (open) that are brighter than $I=25$ in (a) 1455 + 22, (b) 0016 + 16, and (c) 1603 + 43. (d) The $V-I$ colour distribution of the combined field samples from the three clusters, split into the various magnitude slices. The bars at the top show the range of colours covered by the non-evolved morphological types as a function of redshift. The galaxy colours generally start at the left side for $z=0$, and move right until $z\sim 0.5$, at which point they start becoming bluer again.

© Royal Astronomical Society • Provided by the NASA Astrophysics Data System

1994MNRAS.270..245S

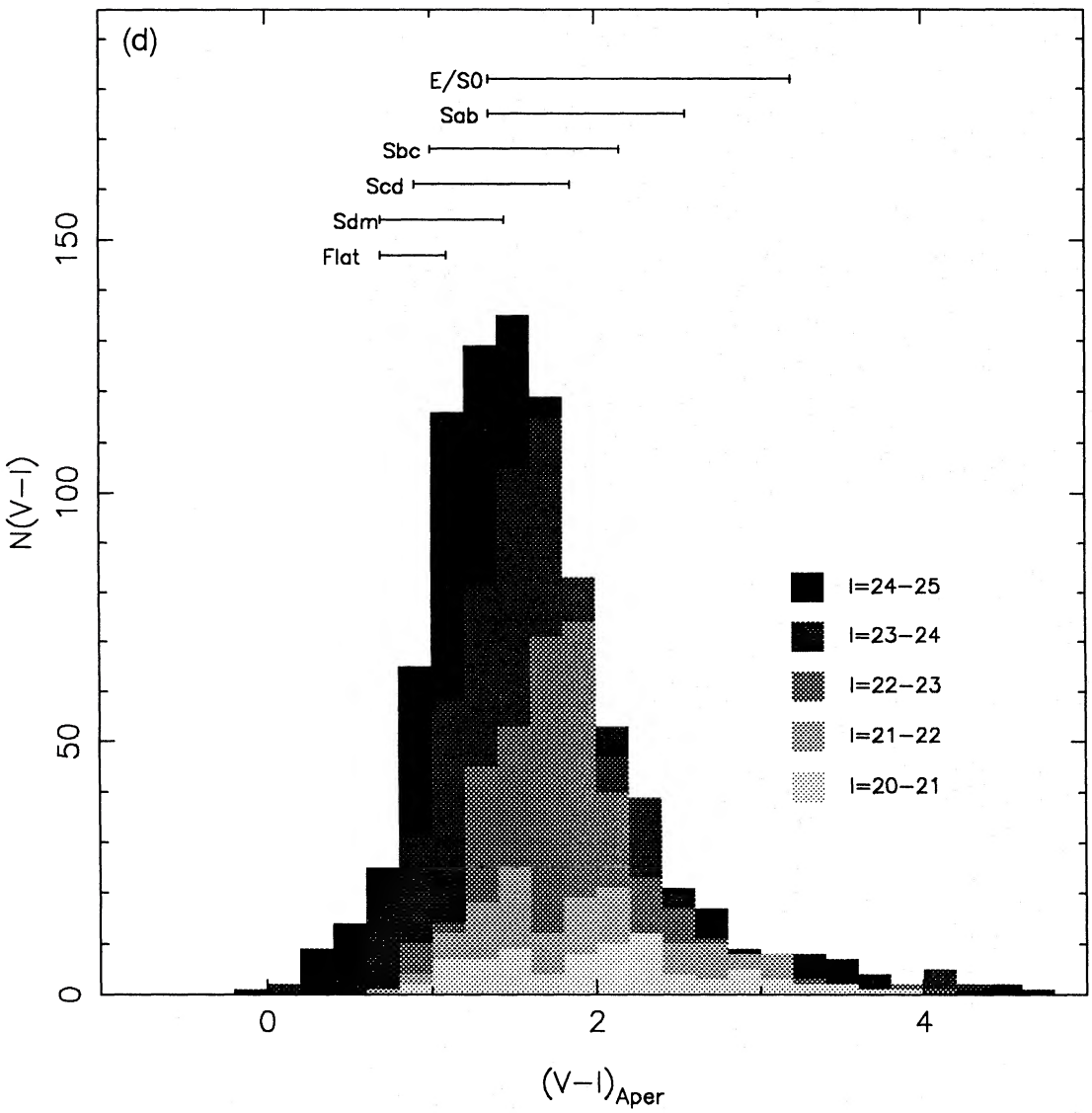

Figure 5 – *continued*

developed by Bower et al., this yields a lower limit on the epoch of formation of cluster ellipticals of $z_{\rm for} \gtrsim 3$ (Ellis 1993).

3.3.3 1603+43 (z = 0.89)

A high-redshift ($z \simeq 1$) cluster was considered essential in our survey, in order to test the possibility of a truly high-redshift ($z \geq 2$) component in the faint counts. Selecting such a cluster presented little difficulty, since very few are known. At the time of its discovery, 1603+43 was the most distant optically selected cluster known. It was discovered by Gunn et al. (1986), and the subsequent spectroscopic follow-up by Dressler & Gunn yielded redshifts for ~5 cluster members, with a mean redshift of $z = 0.895$. The cluster was also included in the study of high-redshift cluster populations by Aragón-Salamanca et al. (1993).

The very long exposure times on the WHT for this target produce faint 80 per cent completeness limits of $I = 25.9$ and $V = 26.3$ (Fig. 2c). The $I = 25$ detection limit corresponds to a 21σ detection within the seeing disc. The colour–magnitude diagram (Fig. 3c) shows that the cluster colour–magnitude relation is broader than in the lower redshift clusters and offset in colour compared to non-evolving ellipticals at $z = 0.89$ (cf. Aragón-Salamanca et al. 1993). An excess of objects can be identified to at least $I = 23.5$. To remove cluster members, we adopted a very broad colour criterion, combined with a faint magnitude cut-off of $I = 24.0$. In this way, we identified 70 cluster galaxies, with 33 in the range $[m_3, m_3 + 2]$, i.e. a richness comparable to Coma. The cluster centre is associated with a prominent 'V' of galaxies and the spatial distribution of members shows a bimodal structure with one peak over the 'V' of galaxies in a frame centre and the second peak lying to the west on the frame border.

This cluster was one of four high-redshift targets from the Gunn et al. (1986) sample, imaged with the *ROSAT* PSPC (Castander et al. 1994). The cluster was detected within a 2×2 arcmin^2 aperture at a 6.5σ significance level, in a total exposure time of 28 ks, corresponding to

© Royal Astronomical Society • Provided by the NASA Astrophysics Data System

1994MNRAS.270..245S

$L_X \simeq 1.1 \pm 0.2 \times 10^{44}$ erg s^{-1}. Given the apparent optical richness of this cluster, from the K-band imaging of Aragón-Salamanca et al., the low X-ray luminosity is somewhat surprising. Castander et al. conjecture that the negative evolution in cluster X-ray properties claimed at low redshift (Edge et al. 1990) continues in more distant samples. Whilst these observations give no indication of the likely concentration of the mass in 1603+43, they do show that it has a much higher X-ray luminosity than many of the lower redshift Couch et al. sample – some of which have gravitational arc candidates (Smail et al. 1991).

The optical richness of this cluster is consistent with the high spectroscopic identification rate for members and, when combined with the X-ray luminosity, provides good evidence that the cluster is massive. In the absence of the strong evolution observed, the low-redshift σ_{cl}–L_X relation would yield a rest-frame 1D velocity dispersion of $\sigma_{cl} \gtrsim 800$ km s^{-1}. If the observed evolution arises from effects other than growth of the cluster potential wells, as has been proposed by Kaiser (1991), then this value is a lower limit to the dark matter's velocity dispersion (the relevant quantity for the lensing studies).

3.4 Field colour–magnitude distributions

Fig. 4 shows the field colour–magnitude distributions constructed by the procedures discussed earlier for each of the three cluster areas. All show the well-known trend to bluer colours at fainter magnitudes. The median colour for the entire field sample brighter than $I=25$ is $V-I=1.55 \pm 0.10$. The lower envelope to the colour distribution is $V-I \sim 0.9$, similar to that of a flat spectrum source. Interestingly, the number of objects with flat spectrum colours increases rapidly beyond $I \sim 23$ ($B \sim 25$). Previous workers (Tyson 1988; Cowie et al. 1989) claimed a discontinuity in the photometric data at about this point. Certainly, the colour distributions brighter and fainter than $I=23$ are highly inconsistent with their having been drawn from the overall parent population. When allowance is made for the bluing of the entire population, however, the shapes of the two distributions are very similar.

The deepest uniform I sample, consistent with the detection limits across the three clusters, is $I_{iso}=25.0$, giving >95 per cent completeness limits in all three clusters. This limit corresponds to a minimum detection significance in the I band of $\sim 17\sigma$ in the seeing disc. When combined with a similar detection requirement in the V frame, this creates a very robust sample with which to work.

3.5 Estimating image parameters of faint field galaxies

Fig. 1 illustrates a random 1×1 arcmin^2 test area taken from the 1455+22 field. The frame contains 40 objects that are brighter than $I_{iso}=25$ in the field, and those with $I_{iso} \in 24$–25 are marked. The lensing technique relies upon our ability to estimate the ellipticities of these faint objects.

The problem of measuring reliable ellipticities for faint objects remains an area of active research. Intensity-weighted second moments (as used in FOCAS) can yield reliable ellipticity and orientation estimates for bright sources but, for the faintest objects under consideration here, the outer isophotes are heavily influenced by noise. For this reason, the intensity-weighted and unweighted moments give very similar results.

To circumvent this, we developed an alternative approach. Instead of using the detection isophote to define pixel membership for an object, we selected a circular aperture and, to reduce the noise from the outer regions, a *radial* weighting function was applied when calculating the second moments in this aperture. The optimal weighting function for a particular object then had the same profile as the object. To simplify matters, we adopted a generic circular Gaussian with a variable width as a weighting function – this simplification has been shown to be reasonable (Bernstein, private communication). The width was determined from the intensity-weighted radius of the object, broadened by convolving with the point spread function. We refer to moments measured using this algorithm as 'optimally weighted'.

Two separate tests were undertaken to estimate the reliability of the ellipticity measurements for the faintest objects in our sample. The first test involved estimating the ellipticity errors of $I=25$ galaxies, using simulations. The second test measured the scatter in an individual measurement from two independent observations of the same field. The simulations consisted of a large number of artificial frames, populated by objects with known ellipticities. For the comparison test, individual exposures comprising the final 1455+22 I frame were combined to create two independent frames, each with a total exposure time of 9.5 ks. These were then analysed and the resulting catalogues matched to allow comparison of the measured image parameters (Fig. 6). Both tests have some drawbacks – the simulation results are dependent upon the form of the galaxy profile used, while the real observations are, of necessity, shallower than the final image.

In the simulations, the intensity-weighted FOCAS moments provide an unbiased and reasonably accurate estimate of the input object ellipticity ($\langle \Delta\varepsilon \rangle = 0.16$). The optimally weighted moments are systematically rounder, by about 0.1, than the input (Fig. 6). The comparison test showed, however, that the optimally weighted moments have a roughly four-fold reduction in the scatter in the ellipticities measured for an object from both frames ($\langle \Delta\varepsilon \rangle = 0.04$ versus $\langle \Delta\varepsilon \rangle = 0.16$ for the objects with $I_{iso} \in 24$–25). A similar reduction in scatter and the introduction of a systematic offset have also been reported by Bernstein (private communication).

In our analysis, we use the more efficient optimally weighted moments for tests where the systematic bias introduced could be modelled (such as the mass mapping presented in Paper II); otherwise the intensity-weighted FOCAS moments were used.

4 STATISTICAL ANALYSES OF GRAVITATIONAL LENSING

4.1 Model redshift distributions

Our primary goal is to use gravitational lensing as a tool to constrain the redshift distribution of faint field galaxies well beyond the spectroscopic limits of the largest current telescopes. As we are mainly concerned with establishing a *statistical* result for the mean distance to the faint population at $I \leq 25$, we have tested our lensing signals against three

© Royal Astronomical Society • Provided by the NASA Astrophysics Data System

1994MNRAS.270..245S

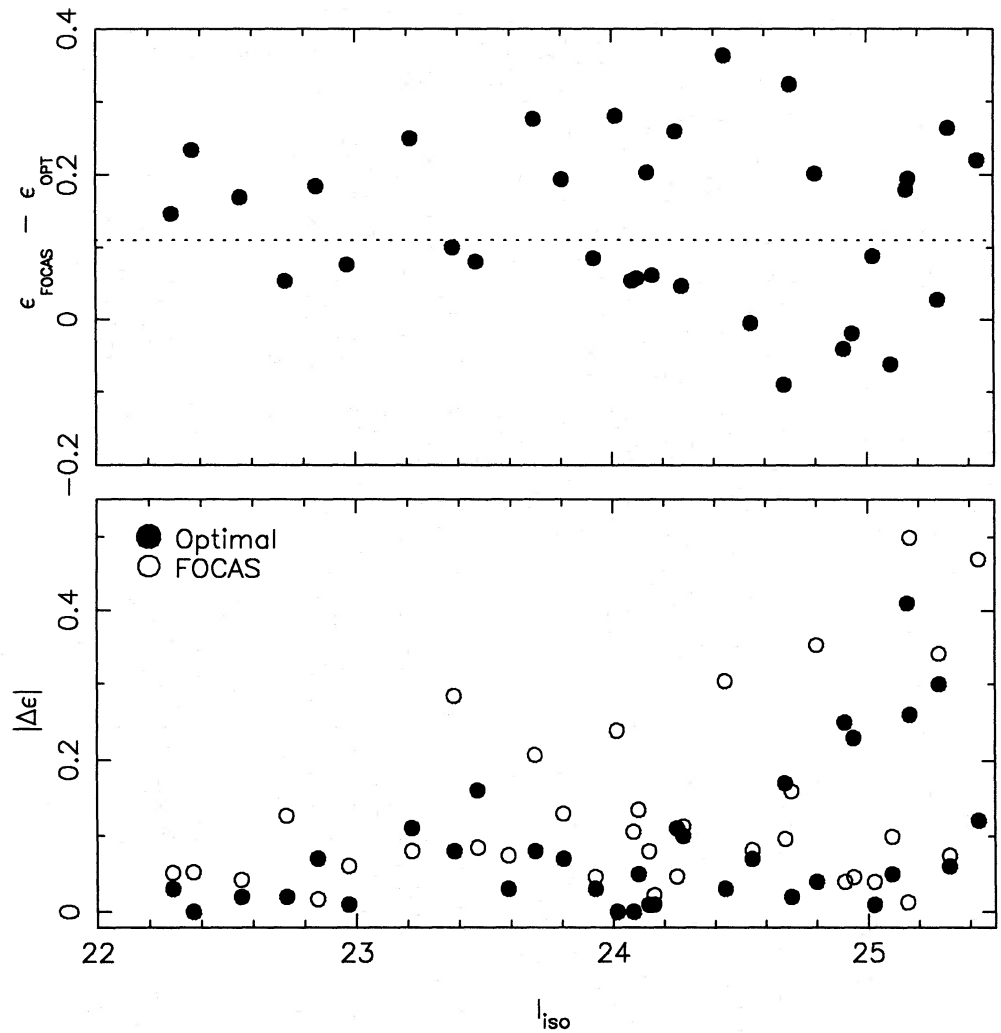

Figure 6. The two panels show the comparison of the raw (FOCAS) and optimally weighted ellipticities for the 1455 + 22 test area. The top panel illustrates the systematic offset (dotted line) introduced in the ellipticity measurement when using the optimal weighting scheme. The lower panel compares the ellipticities of objects measured on the two independent frames. It is apparent that the optimal weighting reduces the scatter in individual ellipticity measurements for $I_{iso} \in [24, 25]$ objects.

model redshift distributions $N(z)$, which encompass the various physical models discussed in Section 1.

The three model distributions adopted for the $I \leq 25$ samples are as follows.

(i) The *no-evolution* ('N.E.'; King & Ellis 1985) prediction, which maintains a reasonable fit to the deepest spectroscopic observations thus far and might be considered an appropriate model for the merger-induced star formation picture (Broadhurst et al. 1992).

(ii) The *shallow* prediction, which maintains the form of the distribution observed at $I = 21$, irrespective of the limiting magnitude. Fainter than $I = 21$, galaxies simply pile up in the same redshift range, as might be expected if there was a well-defined era of recent dwarf formation (Babul & Rees 1992).

(iii) A *deep* prediction, which includes a significant proportion of galaxies with $z > 1$, as originally claimed by Tyson et al. (1990). We adopted the distributions of White & Frenk (1991), which are based on a hierarchical model for galaxy formation and transformed roughly from B to I using a fixed colour term.

The three model redshift distributions are summarized in Fig. 7. The potential of our clusters to distinguish between these models can be examined by considering the proportion of $I \leq 25$ galaxies lying beyond our clusters. For the three model $N(z)$ distributions, the fractions behind 1455 + 22, 0016 + 16 and 1603 + 43 are, respectively, Shallow (63, 1 and 0 per cent), N.E. (96, 69 and 20 per cent) and Deep (97, 83 and 65 per cent). Whilst a continuum of intermediate possibilities is physically plausible, particularly between the no-evolution and deep cases, the three models are, we believe, sufficient for this exploratory study.

4.2 The lensing tests

While image parameters have been determined for statistically complete catalogues of field galaxies in the three cluster areas, we still have to develop algorithms for estimating the

© Royal Astronomical Society • Provided by the NASA Astrophysics Data System

1994MNRAS.270..245S

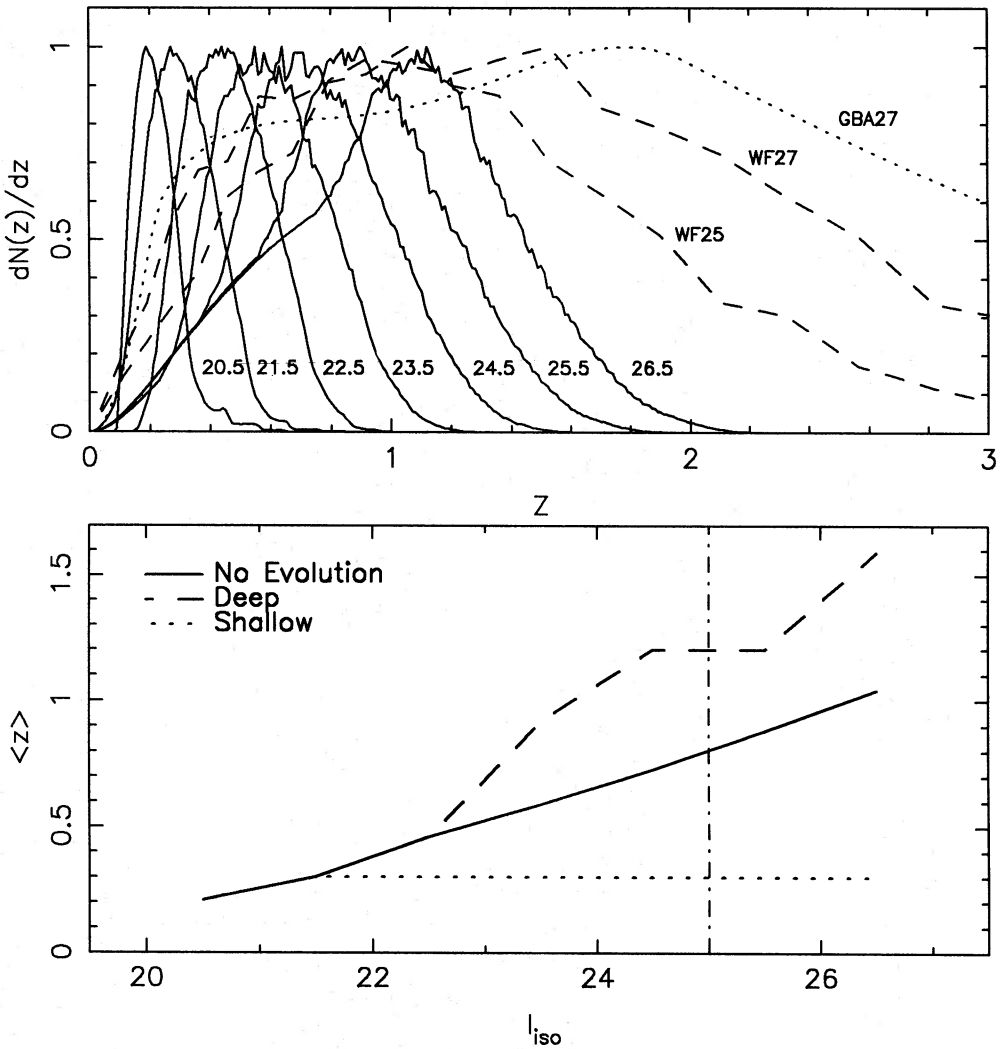

Figure 7. (a) The various normalized redshift distributions used in the analysis. The dashed curves marked WF25 and WF27 are the $B=25$ and $B=27$ distributions from White & Frenk (1991). The curve shown as dotted is a Bruzual $B=27$ cumulative $N(z)$. The remaining solid curves show the no-evolution differential $N(z)$ centred on the I magnitude marked – these were calculated for observations in the R band and then converted using a fixed colour term. (b) The run of median redshift with I magnitude for the three hypotheses.

coherent lensing signal. In recent years, a number of statistical methods have been developed to analyse the weak lensing of faint galaxies by rich clusters (Kochanek 1990; Miralda-Escudé 1991a,b; Kaiser & Squires 1992). In general, these methods aim to derive the mass profile of the lensing cluster, rather than the properties of the faint galaxy population – which are assumed to be known.

The analyses fall into two main classes: parametric likelihood tests, which assume some functional form for the relative mass distribution in the lens and then attempt to determine the most likely values of the model parameters (Kochanek 1990; Miralda-Escudé 1991a,b) and non-parametric tests, from which the 2D projected mass distribution (Kaiser & Squires 1992) can be directly inferred. The former methods are capable of testing the faint galaxy properties, whereas the latter methods are better suited for investigating the *relative* distribution of mass in the lensing cluster.

Throughout this paper we will assume that our lenses can be modelled by a spherically symmetric non-singular isothermal sphere, parametrized by a core radius r_c, and a rest-frame one-dimensionl velocity dispersion σ_{cl}. We chose this simplification initially to make progress in the absence of any other information. As we explained in Section 1, however, the companion article (Paper II) presents the non-parametric analyses using the Kaiser & Squires statistic, and those results allow us to test directly the parametric methods adopted in this paper. The uncertainties in assuming the clusters can be parametrized by simple isothermal models are reviewed in that paper.

4.3 Parametric methods

The parametric tests compare the observed distributions of image parameters with those calculated for a family of lensing clusters for each of the various $N(z)$. These 'model' distributions were first calculated using an *analytic* prescription of the lensing effect of a given cluster, assuming the data to have very simple noise properties. In tests, however, we

© Royal Astronomical Society • Provided by the NASA Astrophysics Data System

1994MNRAS.270..245S

found that, although this method is sensitive to the redshift distributions, it yields cluster parameters that are systematically offset from their true values. This is presumably because the real data contain systematic effects not represented in the analytical treatment. To correct for this degradation, we undertook more realistic *simulations*, which attempt to include all the likely sources of observational noise to estimate, as accurately as possible, the offset in the cluster parameters.

To determine the suitability of a given $N(z)$ for a given set of cluster parameters, we adopted a simple maximum likelihood technique. Consider two redshift distributions, a test hypothesis (say, the deep case) and a null hypothesis (the no-evolution case). For both we estimate the probability that the observed data set for a given cluster can be reproduced according to a family of lens models. The application of the maximum likelihood method to each hypothesis will yield two estimates of σ_{cl}, denoted $\hat{\sigma}_0$ and $\hat{\sigma}_1$, two estimates of r_c ($\hat{r}_{c0}$ and $\hat{r}_{c1}$) and two probabilities, $\hat{p}_0$ and $\hat{p}_1$. These probabilities are determined by comparing the observed image orientations, ellipticities and radial positions from the lens centre with those predicted by the models (cf. Smail et al. 1991). We compare the hypotheses by constructing the likelihood ratio $\Lambda = \hat{p}_0/\hat{p}_1$. If the ratio is large ($\Delta \gg 1$), the alternate hypothesis is rejected in favour of the null hypothesis. This approach can obviously be extended to test the relative likelihoods for our three model $N(z)$. In addition to selecting the most likely $N(z)$, the maximum likelihood method returns preferred values for the lens parameters for each cluster.

4.3.1 *Analytical solutions*

The analytical test works as followed. For each $N(z)$, a combination of core radius and velocity dispersion for the lens are chosen from a grid of values. Galaxies are then drawn randomly from the hypothesized redshift distribution. The model galaxies are distributed uniformly across the source plane, with ellipticities drawn from the observed blank field distribution and random orientations. The image distortion arising from the lens is calculated using the formalism of Miralda-Escudé (1991a), which yields the radial position (r), the orientation relative to the lens centre (θ), and the ellipticity (ε) of the model image. The procedure is repeated until there are sufficient objects to allow a fair comparison of the model distributions with the observations. A linear Kolmogorov–Smirnov test compares the observed and predicted distributions, and the final likelihood that the model could create the observations is determined by combining the probabilities [$\log \hat{p} = \log(p_\varepsilon p_\theta p_r)$]. The test is extremely powerful when applied to strong lensing systems. As the lensing signal diminishes, however, so does its distinguishing power.

Fig. 8 shows how accurately our lensing test can determine the correct input cluster parameters for two different kinds of simulations. Both simulations adopt the observational parameters (cluster redshift, frame size and field galaxy magnitude limit) for the 1455+22 data set and assume, as input, that the cluster is a spherical system with $\sigma_{cl} = 1400$ km s^{-1} and $r_c = 100$ kpc, and the galaxies are drawn from the no-evolution redshift distribution. The logarithmically spaced probability contours show the derived cluster parameters, assuming the observed galaxies to be drawn from either the no-evolution (H_0) or shallow (H_1) redshift distributions. The filled circle denotes the correct input value in the σ–r_c plane. In the top panels, the catalogue was constructed using the analytical formalism of Miralda-Escudé (described above), whereas in the bottom panels the simulations attempt to allow for as many of the observational selection effects as possible, by constructing a realistic *frame* of the simulated cluster (see Section 4.3.2 for a detailed description).

In the case of the analytical models, the test readily returns the correct redshift distribution: the probability ratio is $\log \hat{p}_1/\hat{p}_0 \equiv \log \Lambda < -10$. In addition, the input lens parameters are correctly recovered. The shape of the likelihood contours can be understood in terms of a trade-off between an increase in σ_{cl} – which strengthens the lens – against an increase in r_c – which weakens it. The shifts between the contours for the two redshift distributions arise because more distant galaxies are more easily distorted. Examining the individual distributions, we find that the greatest power comes from the orientations which constrain the solution to lie somewhere along a slanted locus. The ellipticities and radial positions then confine the solution to a point on this locus. Whilst the overall likelihood is derived by assuming that the probabilities from the three K–S tests for r, θ and ε are independent, this is not a critical assumption, given the dominant power of the orientation distribution.

For the catalogue from the simulated frame, the test still correctly distinguishes between the two possible redshift distributions, with $\log \Lambda = -1.8$. However, a systematic offset in the best-fitting lens parameters appears. The calibration and correction for this offset is the motivation for creating simulated frames, and its source is discussed below. The ability of the test to determine the correct lens parameters is very sensitive to the strength of the observed lensing signal. For weak signals, the likelihood peak flattens and, while the test can still determine the correct redshift distribution, the lens parameters become less meaningful.

The analytical catalogue (created in the same manner as the analytic models) obviously disregards a number of complications. The effects of noise on the image measurements and the degradation of the induced distortion by seeing are ignored. Both these effects will introduce a systematic error in the measured ellipticity. However, their effect on the image orientations will be random. By concentrating on the image orientation and radial distributions, it is hoped that the effects of these systematic errors will be minimized. Furthermore, the fixed source magnitude limit results in a paucity of objects in the lens centre on the image plane. This is because amplification bias has been neglected; this acts to populate this region by magnifying galaxies fainter than the observation's magnitude limit into the sample. The combined effect of all these processes is to reduce the observed lensing signal in the simulated frames (Fig. 8). By using simulated observations, this degradation can be calibrated and the observations corrected for it.

4.3.2 *Simulated frames*

To calibrate the statistical tests applied to the real observations, we simulate a set of frames, which are analysed in the same manner as the real data using FOCAS. This approach was

© Royal Astronomical Society • Provided by the NASA Astrophysics Data System

1994MNRAS.270..245S

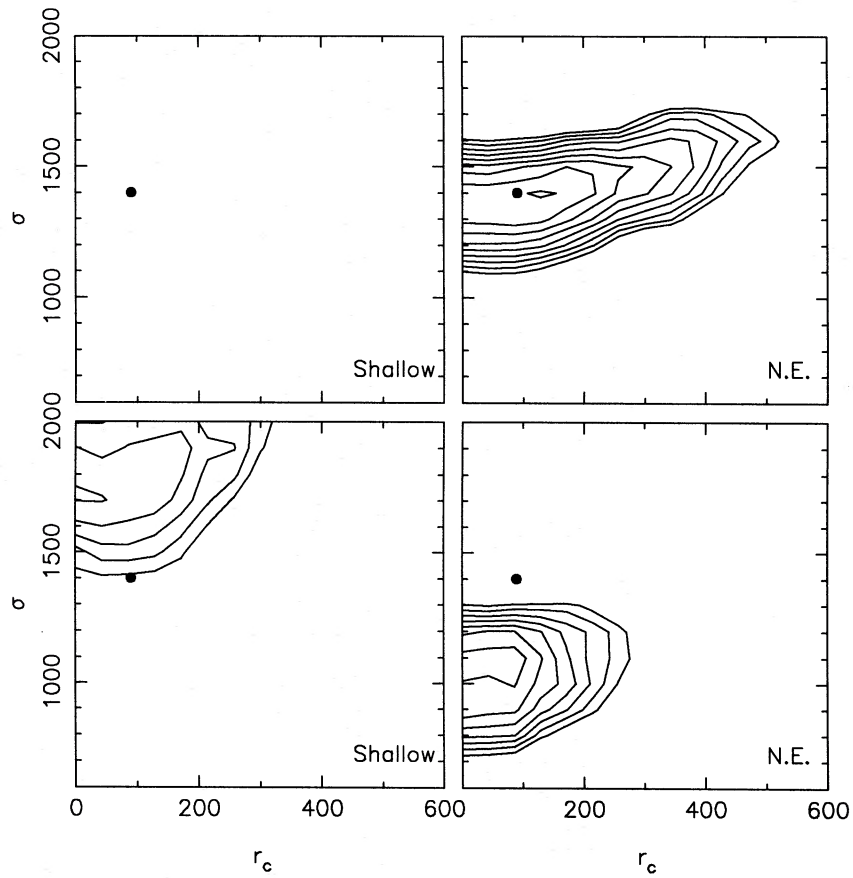

Figure 8. The top panels show the likelihood contours of a test of an analytic simulation, while the bottom panels show the contours for a numerical simulation with the same lens parameters. The probability contours are logarithmic and spaced every factor of 10 – starting at 10^{-10} below the peak probability. Details of the simulations are given in the text, the input redshift distribution was the no-evolution model and the lens parameters are marked (●). The core radius (r_c) is in kpc and the velocity dispersion (σ_{cl}) is in km s^{-1}.

chosen to cater for most of the biases that are likely to occur in the data which cannot be handled analytically. Each of these may degrade the strength of the lensing signal, causing systematic errors in the derived lens parameters. The most obvious effect is atmospheric seeing, but sky noise and undetected merged images also contribute. Underlying correlations in the data due to redshift dependence of certain image characteristics are also a concern, unless properly modelled. The lensing is performed using the same technique as in the analytic simulations with a number of additional features, as follows.

(i) The effects of seeing, pixellation and sky noise on the measurements are included in the simulated image, to match those appropriate for a particular observation.

(ii) Instead of a cumulative $N(z)$ to a given magnitude limit, a differential distribution is used, which allows empirical control of changes to the form of the $N(z)$ as a function of magnitude, allowing us to model easily the effects of amplification bias in our observations. Furthermore, as the distortion at a particular radius on the source plane increases with redshift, more distant sources will tend to be more distorted. However, as the signal to noise in a given ellipticity measurement decreases for fainter objects, it is important that the faintest, possibly most distant, and hence most strongly lensed objects are most effectively degraded. Ideally, we would also like to include any correlation of source size or ellipticity with redshift, but there are currently no observational data on either of these correlations. Images to $I=23$, unaffected by atmospheric seeing, were kindly supplied by the *HST* Medium Deep Survey (MDS) Team, and scale-lengths for sources selected from their first deep image (Griffiths et al. 1992) were measured for this purpose.

(iii) The effects of crowding on image detection and the distortion of image isophotes by undetected faint images are also included. The latter effect is incorporated by lensing galaxies fainter than the adopted magnitude limit (to $I=27$), their number being determined from extrapolating the observed counts. Detected objects fainter than $I=25$ are then discarded after the FOCAS analysis. The sources are uniformly distributed on the source plane, and the inclusion of the fainter sources thus allows modelling of amplification bias. Current data imply a very weak two-point correlation function for such faint objects (Efstathiou et al. 1991; Couch et al. 1993), and so the crowding effects will not be appreciably underestimated.

Of course, once again, there are shortcomings with these simulations. The most obvious is that the technique used to lens the galaxies does not produce any curvature in the final images. This is unimportant for the majority of images, but rare strongly lensed images (giant arcs) close to the cluster

© Royal Astronomical Society • Provided by the NASA Astrophysics Data System

1994MNRAS.270..245S

centre are not well modelled. None of the three data sets contains such a giant arc and so an upper ellipticity cut-off can be applied to both the simulations and real data to remove this effect. A lower cut-off is already applied due to the intrinsic scatter in the orientation measurements of near circular images.

A potential worry is that we rely on an *ellipticity* distribution taken from ground-based data limited at $I \sim 23$ and taken in $\simeq 1$-arcsec seeing (Colless & Ellis's unpublished NTT data). Clearly, there could be some degradation of the source ellipticities. Although the *HST* MDS data cover a smaller area, a two-sample K–S test shows an 85 per cent probability that the two ellipticity distributions came from the same parent population.

Finally, there is the question of the accuracy of the scale-length distribution used. A similar concern arises in the observations of giant arcs (Wu & Hammer 1993; Smail et al. 1993). Unfortunately, the small area and brighter limiting magnitude of the MDS data make a definitive statement impossible. The derived scalelengths from the *HST* data ($r \sim$ 0.3–0.7 arcsec at $I = 23$) are comparable to those measured from the cluster observations when allowance has been made for the effect of seeing. When applied to the fainter $I \sim 25$ sample, this technique gives a similar range of scale sizes. This quantifies the visual impression that the model faint galaxy images appear very similar to the real data.

In the presence of a strong intrinsic lensing signal, the observational effects listed above appear to bias only the derived velocity dispersion of the cluster, while returning a good estimate of the input core radius. The measured bias then amounts to a velocity dispersion offset of -300–400 km s^{-1} between the input and output cluster parameters, and no offset in the derived core radius. For weak lenses it becomes increasingly difficult to distinguish the offset, because of the weak differentiation between the allowed model parameters.

5 RESULTS AND DISCUSSION

In discussing the results, we will first present the basic evidence for gravitational lensing in our sample, and examine its dependence on the colour of the faint field population. Here, we will essentially follow the original method used by Tyson et al. (1990) and utilize the orientations of faint galaxies perpendicular to the cluster radius vector. Some constraints on the mean redshift of the $I \leq 25$ sample are possible from this analysis, particularly if we introduce mass estimates for 1455 + 22 from X-ray studies. We then apply the more rigorous maximum likelihood analysis to examine the data sets for all three clusters, in the context of the three model $N(z)$ discussed in Section 4. The strength with which we can rule out various redshift distributions depends on how much freedom we are willing to assign to the cluster parameters. The reader is again referred to the companion article (Paper II) for further information.

5.1 Orientation histograms

Tyson et al. (1990) introduced the simple test of measuring the fraction of galaxies aligned tangentially to the cluster radius vector. We start by analysing such histograms for each of the clusters in turn. Making the gross simplification that our clusters are identical objects, and ignoring amplification bias, we directly infer the fraction of galaxies behind each cluster and, hence, $N(z)$.

We select galaxies in elliptical annuli that are aligned with those defined by the cluster members (see Paper II) in order to remove the effect of the lens ellipticity on the orientation histogram. The centres used are the optically defined centres of the clusters. Paper II demonstrates that these centres are consistent with those defined by both the mass and X-ray gas distributions in our cluster sample. Fig. 9 shows the resulting orientation histograms for the $I \leq 25$ field samples, for each of the three clusters. Both the lower redshift clusters show an obvious excess of tangentially aligned images. In 1455 + 22, the excess is approximately 190 in a total of 810 objects (23 ± 2 per cent), corresponding to a surface density of 7.0 galaxies arcmin^{-2}, whereas, for 0016 + 16, it is $\simeq 80$ out of 356 galaxies (21 ± 2 per cent) or 4.5 arcmin^{-2}. 1603 + 43 shows no alignment excess.

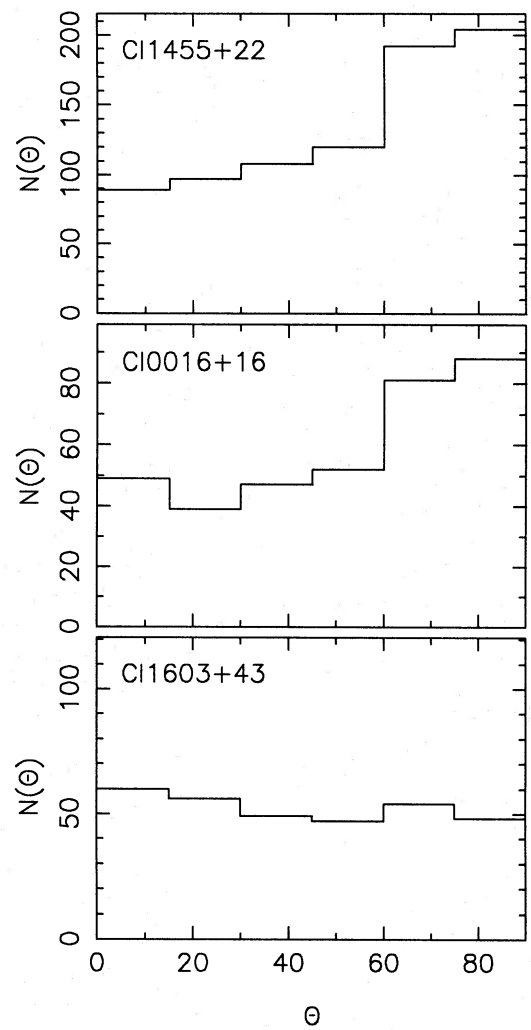

Figure 9. Orientation histograms for 1455 + 22, 0016 + 16 and 1603 + 43. The histograms were constructed using all objects in the field samples with $I \in [20, 25]$ and $(V - I) \in [-1, 2.5]$, with optimally weighted ellipticities above a cut-off of $\varepsilon \geq 0.05$. The orientations and ellipticities used for the annular bins were those quoted in the text and the optically determined lens centres were used.

© Royal Astronomical Society • Provided by the NASA Astrophysics Data System

1994MNRAS.270..245S

Under the assumption of identical clusters, we can compare these orientation histograms with our three hypothetical $N(z)$ distributions. Although considerably idealized, this is illustrative in determining which cluster is the most critical in estimating $N(z)$. Using a K–S test to compare the real and analytical orientation distributions, we rule out the Shallow distribution at the 99.7 per cent level, using the combined result from all three clusters. As expected, 0016+16 provides by far the strongest rejection since, according to the Shallow $N(z)$, only 2 per cent of the $I \leq 25$ population should be beyond $z = 0.55$. Were 1603+43 to be as massive and concentrated as the other clusters, the data would also rule out the Deep $N(z)$.

The signal in the two lower redshift clusters is sufficiently strong that we can subdivide the sample to check Tyson et al.'s claim that the excess is predominantly seen in the bluest or faintest galaxies. We note, however, that, by virtue of using the EEV CCD, we only have a $V-I$ baseline, compared to Tyson et al.'s $B-R$. We chose to split the samples at the mean sample colour of $V-I = 1.5$ and $I_{\rm iso} = 23$ – where the colour distribution rapidly begins to shift to the blue (Fig. 5d).

The orientation histograms for the four subclasses are shown in Fig. 10(a), for 1455+22, and Fig. 10(b), for 0016+16. Clearly all four subclasses, for both clusters, show similar alignments and so we cannot improve the signal contrast by applying photometric selections. The photometric distributions of galaxies in the aligned bins ($\theta > 60°$) are completely consistent with those in the unaligned bins. Indeed, for 1455+22, the two most obvious arclets have colours that fall either side of that of the cluster members, and the radial distribution of the aligned component shows no variation of colour with radius.

We can place a strict limit on the maximum possible colour difference for the *excess* aligned population, if we assume that they are drawn from a population with a colour distribution similar in shape to that observed in the unaligned bins, but shifted to the blue. The upper limits then refer to the maximum colour shift allowed. For 1455+22, the 90 per cent confidence limit is $\Delta(V-I) = -0.2$ and, for 0016+16, it is also $\Delta(V-I) = -0.2$. In other words, the aligned component cannot be drawn from a population that is much bluer in $V-I$ than the main population. Alternatively, the strong shift to the blue seen in the field colours beyond $I = 23$ is not primarily due to the existence of a distant blue $z \gtrsim 1$ galaxy population. This constraint argues against generic Deep models containing a primordial population of distant star-forming galaxies, unless they exhibit a wide spread in $V-I$ colours.

5.2 Constraints from current spectroscopic surveys

The relatively strong alignment signal in the samples brighter than $I = 23$ prompts us to consider a 'boot-strap' method for determining the redshift of the faint galaxy population. If we can measure the lens parameters for a bright sample, for which the field redshift distribution is already secure from conventional spectroscopy, we can then apply the lens model to derive the median redshift of the $I \leq 25$ sample.

At the current time, the deepest I-selected field surveys are those of Lilly (1993) and Tresse et al. (1993), limited at $I \leq 22$. To undertake this analysis, we selected galaxies in 1455+22 and 0016+16, satisfying $I \in [20, 22]$ and $\varepsilon_{\rm opt} \geq 0.05$. To test the method, we chose two input redshift distributions: the one observed by Lilly (hypothesis: H_0) and the Shallow distribution (hypothesis: H_1). We applied a combined maximum likelihood estimator on the radial distribution and orientations and, as expected, 0016+16 is the better discriminator. Taking both clusters, the Shallow redshift distribution was rejected at the 95 per cent level to this apparent magnitude limit. The maximum likelihood parameters for the 1455+22 lens were $\sigma_{\rm cl} = 1300$ km s^{-1} and $r_{\rm c} = 400$ kpc, with $\log \hat{p}_0 = -0.1$. For 0016+16, $\sigma_{\rm cl} = 1800$ km s^{-1} and $r_{\rm c} = 70$ kpc, with $\log \hat{p}_0 = -1.9$. As these estimates are derived from the analysis of a sample of bright galaxies, they are less affected by the systematic biases detailed in Section 4.3.

The uncertain cluster parameters inferred from the small samples that overlap in apparent magnitude with the current spectroscopic redshift surveys indicate that this 'boot-strap' technique is probably too hazardous a method for estimating $N(z)$ to $I \leq 25$. We will see later, however, that the derived cluster parameters are not that erroneous. The prospect of deeper surveys (and thus higher galaxy surface densities) from 10-m class telescopes will make the 'boot-strap' method a viable approach in future.

5.3 Maximum likelihood analyses

We now apply the likelihood analysis described in Section 4.3 to the data sets constructed from the three clusters. We use the complete $I \in [20, 25]$ samples, restricting the FOCAS ellipticities to $\varepsilon \in [0.1, 0.8]$. The likelihood test compares the observed r, θ, ε distributions with those from 10 combined realizations of each lens model calculated for each of the three model $N(z)$. The parameter space searched is $\sigma_{\rm cl} \in [400, 2000]$ km s^{-1} and $r_{\rm c} \in [0, 2]$ arcmin. The upper limit on the core radius translates into metric radii of 0.6, 0.9 and 1.0 Mpc, for the three clusters. The rather small lower limit for the cluster velocity dispersion protects against the probability peak moving outside our searched parameter range, due to the degradation illustrated in Fig. 8.

For 1455+22, the likelihood distributions (Fig. 11a) have very similar shapes to those seen in the simulations presented earlier (Fig. 8). The maximum probabilities for the three redshift distributions are $\hat{p}_{\rm Shallow} = -1.1$, $\hat{p}_{\rm NE} = -0.7$ and $\hat{p}_{\rm Deep} = -0.8$. Thus, the no-evolution $N(z)$ is marginally preferred. The lens parameters for this fit are $\sigma_{\rm cl} = 630 \pm 150$ km s^{-1} and $r_{\rm c} = 210 \pm 100$ kpc. The best-fitting velocity dispersion is strictly a lower limit to the actual value, due to the systematic effects illustrated in the simulations above. The errors quoted are 90 per cent confidence limits, taking the errors in $\sigma_{\rm cl}$ and $r_{\rm c}$ to be orthogonal.

As before, 0016+16 (Fig. 11b) provides the most significant constraint. Here, we obtain $\hat{p}_{\rm Shallow} = -6.2$, $\hat{p}_{\rm NE} = -2.8$ and $\hat{p}_{\rm Deep} = -3.3$, ruling out the Shallow model and again preferring the no-evolution $N(z)$. The lens parameters for the N.E. fit are $\sigma_{\rm cl} = 860 \pm 250$ km s^{-1} and $r_{\rm c} = 210 \pm 250$ kpc, where, again, $\sigma_{\rm cl}$ represents a lower limit to the actual value.

For 1603+43, the three models have maximum probabilities of $\hat{p}_{\rm Shallow} = -1.2$, $\hat{p}_{\rm NE} = -1.3$ and $\hat{p}_{\rm Deep} = -1.4$. Given the uncertain cluster mass, a very wide parameter space was searched. For the N.E. model, a large parameter space is compatible with the observations (Fig. 11c). For

© Royal Astronomical Society • Provided by the NASA Astrophysics Data System

1994MNRAS.270..245S

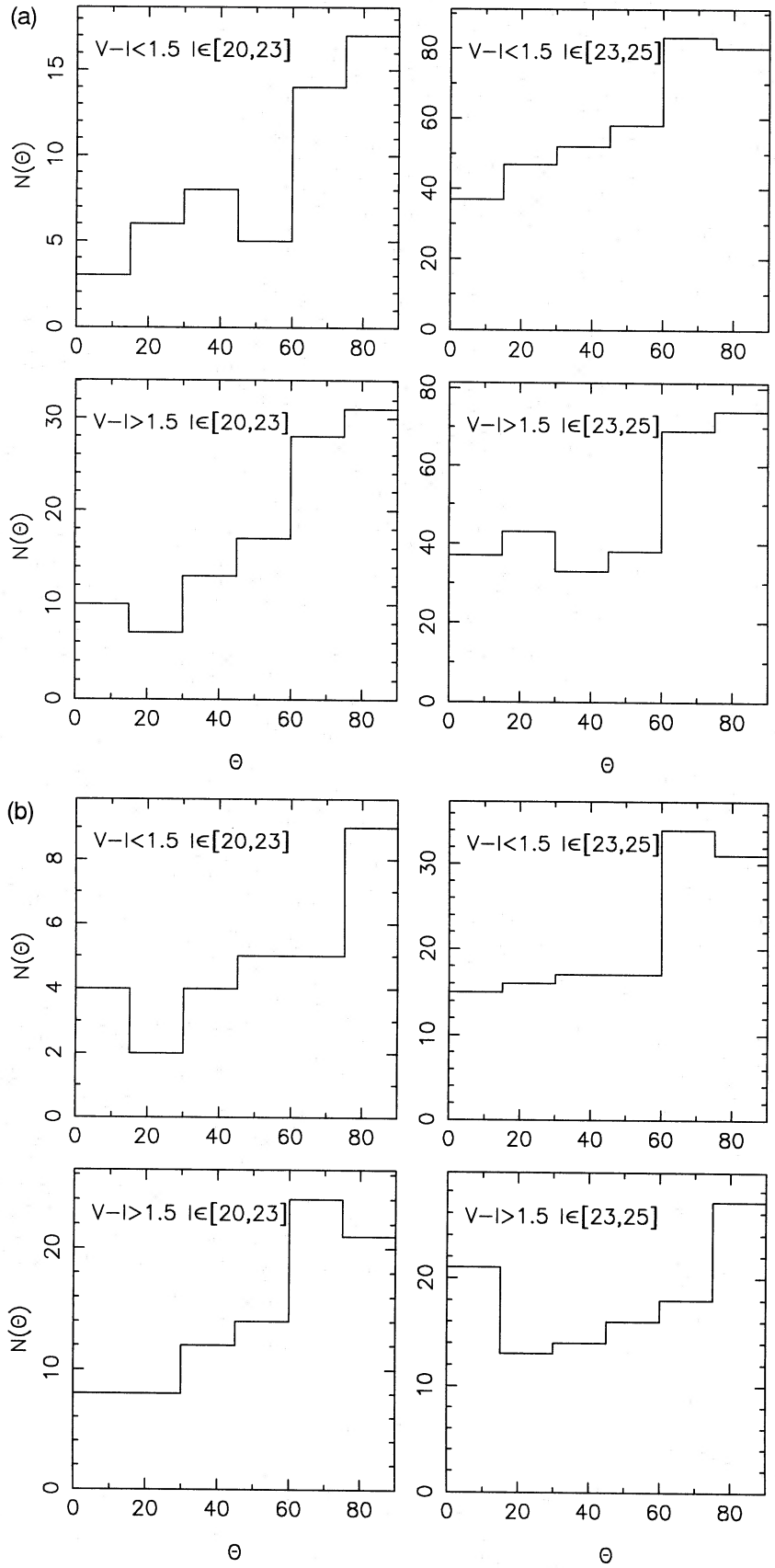

Figure 10. (a) The orientation histograms for 1455 + 22 separated in terms of colour and magnitude. The aligned excess has a similar strength in all four samples, showing that it has no strong colour or magnitude dependence. (b) As above, for the 0016 + 16 sample. As in (a), all four samples contain an excess of tangentially aligned objects, confirming that this arises from a population of objects with similar characteristics to the bulk of the faint field population.

© Royal Astronomical Society • Provided by the NASA Astrophysics Data System

1994MNRAS.270..245S

both the N.E. and Deep models, we obtain $\sigma_{cl} \simeq 400$ km s^{-1} and $r_c \simeq 900$ kpc for the maximum likelihood solutions. It is apparent from Fig. 11(c), however, that, if a lower limit were placed on the velocity dispersion of this cluster or an upper limit were placed on its core radius, we would strongly reject the Deep redshift distribution.

Combining all three clusters, we can reject the Shallow redshift distribution at the 99.98 per cent level ($3.8\,\sigma$), but, without further assumptions about the cluster properties, we can only claim a marginal preference for the N.E. model over the Deep distribution at the level of 23 per cent ($1.2\,\sigma$).

We can refine the derived cluster parameters for the lower redshift clusters from simulated frames (Section 4.3.2). The relatively strong signal in these systems gives a well-determined transformation. From the likelihood fits for the no-evolution $N(z)$, we already have lower bounds of $\sigma_{cl} \sim 600$ and 850 km s^{-1} for 1455+22 and 0016+16, respectively. We simulated images for a family of clusters with different lens parameters (σ_{cl}, r_c) at the two cluster redshifts ($z=0.26$, $z=0.55$), using the N.E. redshift distribution. The likelihood analysis was then run on FOCAS catalogues created from each of these images and the input

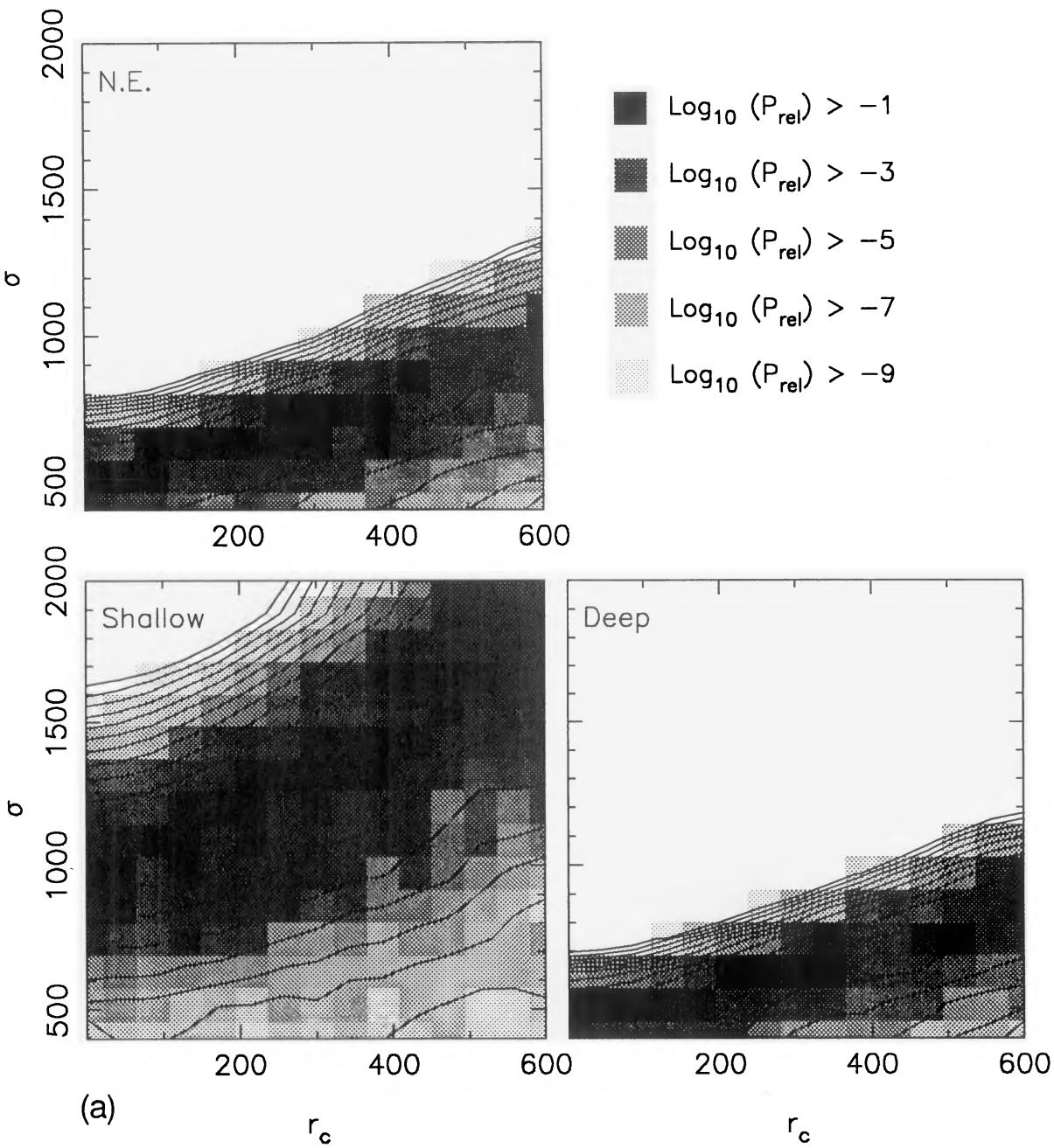

Figure 11. The likelihood distributions for the cluster lensing models of (a) 1455+22, (b) 0016+16, and (c) 1603+43. Each plot is for one of the model redshift distributions. The units for the axes are km s^{-1} and kpc. The contours are for the smoothed probability distributions and are spaced every factor of 10 from the peak.

© Royal Astronomical Society • Provided by the NASA Astrophysics Data System

1994MNRAS.270..245S

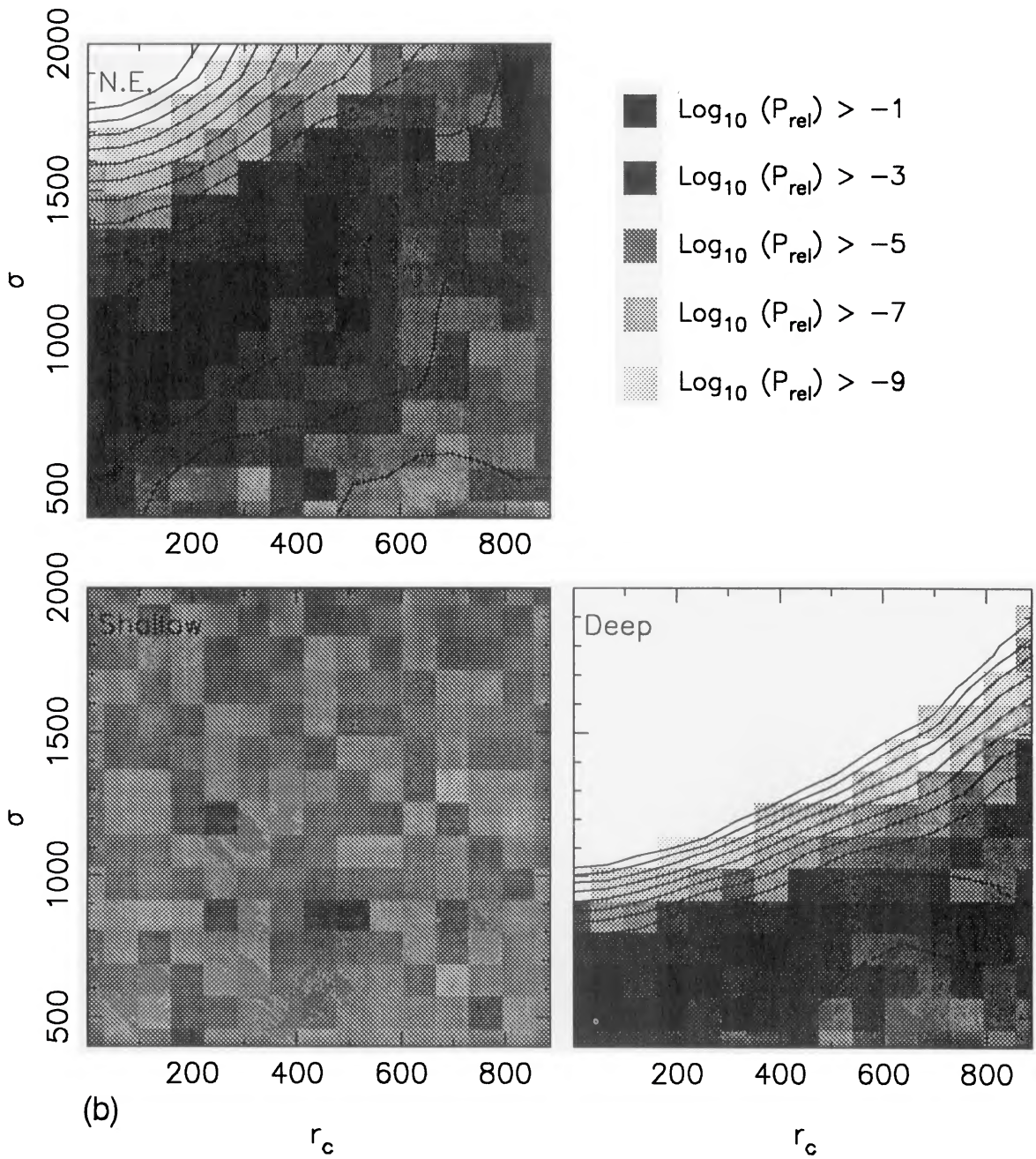

Figure 11 – *continued*

lens parameters of the simulation whose measured parameters are closest to those observed then provide the final corrected estimates of σ_{cl} and r_c for the two clusters.

For 1455+22, the simulation whose derived lens parameters lay closest to the observations had $\sigma_{cl}=1000$ km s^{-1} and a core radius of $r_c=300$ kpc as input. The systematic offset of −300–400 km s^{-1} in the dispersion is similar to that shown in Fig. 8. However, as before, the best-fitting core radius appears to be representative of the intrinsic core size. Singular potentials do not appear to be able to create the observed lens parameters for a reasonable choice of input parameters. The cluster velocity dispersion is below that inferred from the X-ray data but above the spectroscopic value.

In 0016+16, the closest matched simulation has an input dispersion of $\sigma_{cl}=1200$ km s^{-1} and a core radius $r_c=300$ kpc. Again, singular models fail to reproduce the observed lens parameter values. The systematic offset in σ_{cl} is close to +400 km s^{-1} and r_c is in rough agreement with those previously calculated for both the mass and galaxy distributions. The corrected velocity dispersion is gratifyingly close to the spectroscopic value measured by Dressler & Gunn (1992).

5.4 Redshift distributions

Our primary conclusion is the rejection of a redshift distribution to $I\leq 25$ that is significantly *shallower* than the no-

© Royal Astronomical Society • Provided by the NASA Astrophysics Data System

1994MNRAS.270..245S

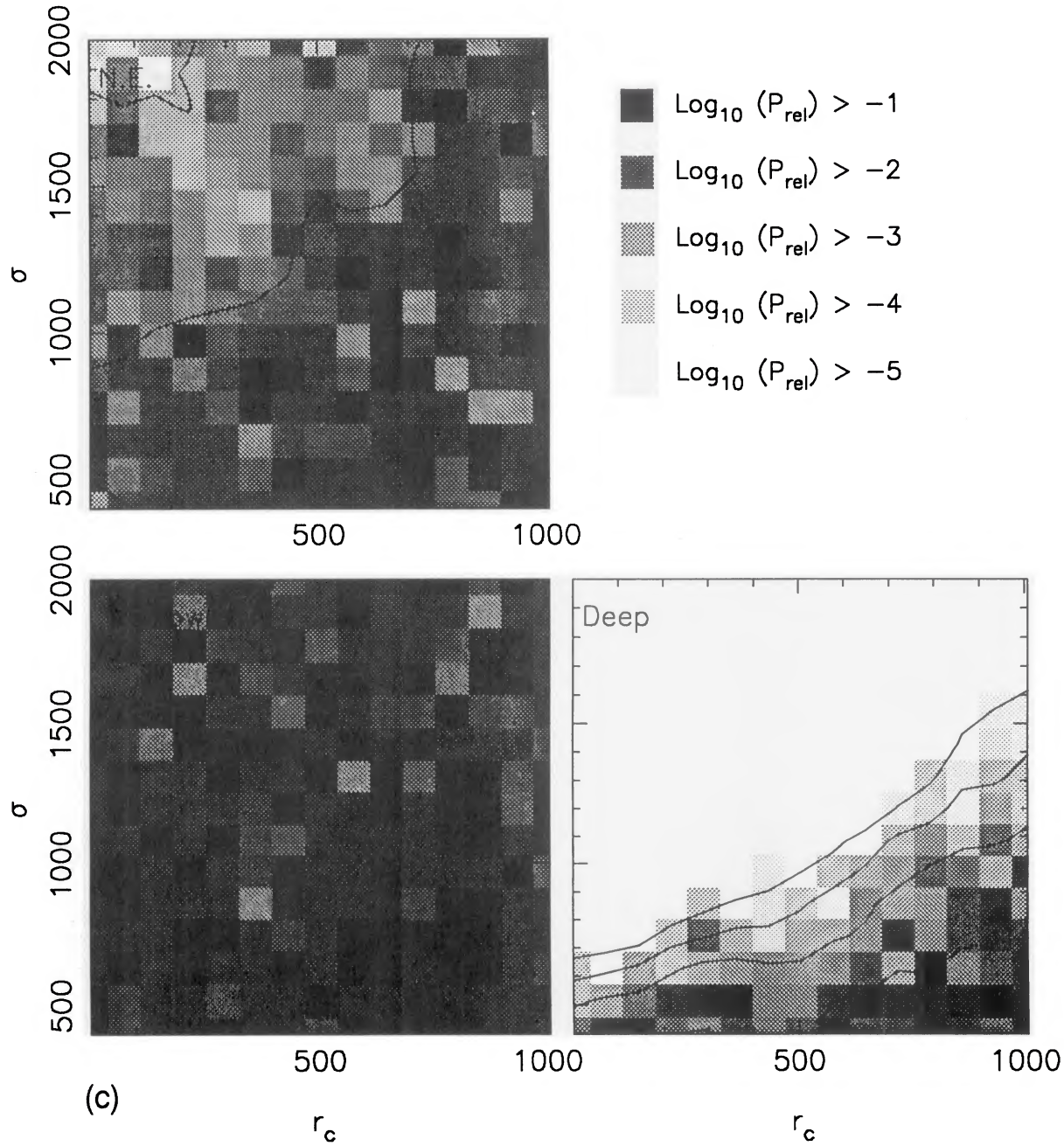

Figure 11 – *continued*

evolution prediction. Such a model would be expected if the ultrafaint counts were dominated by a population of low-redshift ($z<0.5$) dwarfs. The detailed dynamical and/or X-ray data on our two lower redshift clusters, endorsed by the lensing maps presented in Paper II, make this a very robust conclusion. The lensing signal seen in 0016+16 alone is consistent with the bulk (70–80 per cent) of the field galaxies to $I\leq 25$ lying beyond the cluster ($z\gtrsim 0.6$).

To constrain redshift distributions *deeper* than the no-evolution form, we have to consider our most distant cluster, 1603+43. While less information is available about this cluster than for the two lower redshift systems, precision data are not so important, as *any* lensing signal would indicate the presence of a distant population ($z\gtrsim 2$) to $I\leq 25$. The absence of any signal suggests that a substantial (>20 per cent) tail beyond $z\simeq 2$ [such as implied in the White & Frenk (1991) model] is unlikely. To reject formally a high-redshift component at any level, however, a lower limit is needed on the velocity dispersion of 1603+43. At present, this can only be derived from X-ray observations, which, interpreted in terms of low-redshift correlations, predict $\sigma_{cl}>800$ km s^{-1} for an assumed $r_c<250$ kpc. Adopting the nominal offset to the model velocity dispersions discussed in Section 4.3.2, these parameters for 1603+43 would allow us to reject the 20 per cent $z>2$ tail, at a confidence limit of >95 per cent.

Support for our conclusions of an absence of a high-z component to the $I\leq 25$ ($B\lesssim 27$) redshift distribution is provided by the redshift distribution recently derived by

© Royal Astronomical Society • Provided by the NASA Astrophysics Data System

1994MNRAS.270..245S

Kneib et al. (1994), for ~40 arclets seen through the rich cluster Abell 370. The median redshift they obtain for their sample is $z \sim 0.9$, very close to that of the no-evolution model (Fig. 7). Only 15 per cent of their 'best' sample have $z \geq 1.5$.

We can compare the derived line-of-sight velocity dispersions for the two lower redshift clusters with the predicted distribution from the CDM simulations of Frenk et al. (1990), rescaled to $b = 1$ in line with the *COBE* observations. The high inferred velocity dispersions of the clusters, especially for 0016+16 [in both $N(z)$ cases], given its redshift, are at the extremes of the standard cold dark matter predictions. This is particularly interesting, as the derived dispersions are free of the projection effects commonly invoked to force agreement between the predicted cluster velocity dispersion distribution and that observed locally with spectroscopic samples. This discussion is extended in Paper II, where we compare the 2D distributions of the baryonic and total mass in our clusters. We conclude here, however, that selection of clusters according to X-ray luminosity does provide massive systems, although the absence of strongly lensed arcs in these two high-dispersion clusters implies that X-ray selection does not necessarily guarantee a potential compact enough to produce a giant arc.

Although our results rely, to some extent, on the nature of the clusters used as lenses, we demonstrate in Paper II that the mass distribution assumed for the two lower redshift systems can be directly checked from the lensing data, with satisfactory conclusions. The prospects, with 8–10 m telescopes, for improving our understanding of the dynamical state of 1603+43 via ≃30–50 redshifts (such as are available for 0016+16) and for enlarging the overlap between lensing-based and spectroscopically based field redshift distributions (Section 5.2) are excellent. We can thus look forward to tighter constraints on the statistical distances to faint galaxies in the near future.

6 CONCLUSIONS

We have developed new and powerful lensing techniques that are able, with some limitations, to constrain simultaneously the statistical distances $N(z)$ to the field population, at limits well beyond the reach of current spectrographs, *and* the distribution of dark matter in a non-parametric manner. The latter conclusions are discussed in more detail in the companion article, Paper II. We describe detailed tests of these techniques which, we believe, ensure that systematic biases inherent in our observational data sets are well understood.

Our conclusions at this stage can be summarized as follows.

(i) The strongest constraint we can provide on the redshift distribution of a sample of $I \leq 25$ field galaxies is the absence of a significant population of faint low-z dwarfs, such as might be expected if either the faint end of the local galaxy luminosity function is seriously underestimated (cf. Koo et al. 1993) or if there is strong evolution of the faint-end slope at low redshifts. We reject a model $N(z)$ with 98 per cent of the $I = 25$ population at $z \leq 0.55$, at the 99.98 per cent level. The very deep surface brightness limit of our imaging data makes this a particularly effective constraint.

(ii) Our constraints on models with large fractions of high-redshift galaxies are weaker, due to the lack of detailed information about the dynamical state of our most distant cluster 1603+43. Further study of this system and the properties of other high-z clusters is necessary to make progress. At present, we are unable formally to reject models with as high as 20 per cent of the $I \leq 25$ population at $z \sim 2$. However, if, as we surmise from its X-ray properties, 1603+43 is compact and massive, we can reject the Deep model at better than a 95 per cent confidence level.

(iii) By incorporating external constraints on the likely range of parameters for the three clusters, our preferred redshift distribution is therefore the no-evolution model. We might understand how such a model occurs, notwithstanding the high number counts, if the galaxy luminosity function evolves in shape according to the empirical form described by Broadhurst et al. (1988, see their fig. 4). A possible astrophysical model of such evolution, incorporating mergers of fragments whose star formation rate is slowly declining, has been described by Broadhurst et al. (1992).

(iv) The lensing strength of our two lower redshift clusters provides a direct measure of the probable velocity dispersion (σ_{cl}) and core radii (r_c). The estimates, however, particularly σ_{cl}, are affected by systematic biases. Using detailed simulations, we correct the biases and, for 1455+22, obtain $\sigma_{cl} = 1000 \pm 200$ km s^{-1} (compared to the spectroscopic value of ~700 km s^{-1}), and, for 0016+16, we obtain $\sigma_{cl} = 1200 \pm 300$ km s^{-1} (compared to the spectroscopic value of 1300 km s^{-1}). We attempt to derive constraints on the cluster parameters using the lensing signal to $I \leq 22$, where the field $N(z)$ is already well understood from redshift surveys. Whilst the values derived are consistent with those above, no improved estimates are obtained, due to the low surface density of galaxies available at the current spectroscopic limit. We conclude that both clusters are on the extreme tail of the predicted distribution of cluster dispersions in standard CDM (Frenk et al. 1990).

ACKNOWLEDGMENTS

The above project was initiated with inspiration derived from the enthusiasm of Bernard Fort, Yannick Mellier and Genevieve Soucail at Toulouse Observatory, and the pioneering work of Tony Tyson and colleagues. We acknowledge useful discussions with Gary Bernstein, Carlos Frenk, Nick Kaiser, Chris Kochanek and Jordi Miralda-Escudé. The support of the La Palma staff, and especially Dave Carter, is also gratefully acknowledged. This work was supported by the SERC.

REFERENCES

Abell G. O., Corwin H. G., Olowin R. P., 1988, ApJS, 70, 1
Allington-Smith J. R. et al., 1994, MNRAS, in press
Aragón-Salamanca A., Ellis R. S., Couch W. J., Carter D., 1993, MNRAS, 262, 764
Babul A., Rees M. J., 1992, MNRAS, 255, 346
Birkinshaw M., Gull S. F., Hardbeck H. E., Moffatt A. T., 1994, ApJ, submitted
Bower R. G., Lucey J. R., Ellis R. S., 1992, MNRAS, 254, 601

© Royal Astronomical Society • Provided by the NASA Astrophysics Data System

1994MNRAS.270..245S

Broadhurst T. J., Ellis R. S., Shanks T., 1988, MNRAS, 235, 827
Broadhurst T. J., Ellis R. S., Glazebrook K., 1992, Nat, 355, 55
Castander F., Ellis R. S., Frenk C. S., Dressler A., Gunn J. E., 1994, ApJ, 424, L79
Cole S., Ellis R. S., Colless M., Broadhurst T. J., 1993, MNRAS, 267, 541
Colless M., Ellis R. S., Taylor K., Hook R. N., 1990, MNRAS, 224, 408
Colless M., Ellis R. S., Broadhurst T. J., Taylor K., Peterson B. A., 1993, MNRAS, 261, 19
Colless M., Schade D. J., Broadhurst T. J., Ellis R. S., 1994, MNRAS, 267, 1108
Couch W. J., Ellis R. S., Malin D. F., MacLaren I., 1991, MNRAS, 249, 606
Couch W. J., Jurcevic J. S., Boyle B. J., 1993, MNRAS, 264, 604
Cowie L. L., 1991, in Shanks T. et al., eds, Observational Tests of Cosmological Inflation. Kluwer, Dordrecht, p. 257
Cowie L. L., Lilly S. J., Gardner J., MacLean I., 1989, ApJ, 332, L29
Cowie L. L., Songaila A., Hu E. M., 1991, Nat, 354, 460
Dressler A., Gunn J. E., 1992, ApJS, 75, 1
Edge A., Stewart S., Fabian A., Arnaud K. A., 1990, MNRAS, 245, 559
Efstathiou G., Bernstein G., Katz N., Tyson J. A., Guhathakurta P., 1991, ApJ, 380, L47
Ellis R. S., 1993, in Akerlof C. W., Srednicki M. A., eds, Texas/PASCOS '92 Relativistic Astrophysics & Particle Cosmology, Ann. NY Acad. Sci., 688, p. 207
Ellis R. S., Couch W. J., MacLaren I., Koo D. C., 1985, MNRAS, 217, 239
Frenk C. S., White S. D. M., Efstathiou G., Davis M., 1990, ApJ, 351, 10
Glazebrook K., Ellis R. S., Colless M., Broadhurst T. J., Allington-Smith J., Tanvir N., Taylor K., 1994, MNRAS, in press
Griffiths R. et al., 1992, in Benvenuti P., Schreier E., eds, Proc. ST-ECF/STScI Workshop, Science with the Hubble Space Telescope. p. 13
Grossman S. A., Narayan R., 1988, ApJ, 324, L1
Gunn J. E., Hoessel J. G., Oke J. B., 1986, ApJ, 306, 30
Henry J. P., Gioia I. M., Maccacaro T., Morris S. L., Stocke J. T., Wolter A., 1992, ApJ, 386, 408
Jarvis J. F., Tyson J. A., 1981, AJ, 86, 476
Kaiser N., 1991, ApJ, 383, 104
Kaiser N., Squires G., 1992, ApJ, 404, 441
King C. R., Ellis R. S., 1985, ApJ, 288, 456
Kneib J.-P., Mathez G., Fort B., Mellier Y., Soucail G., Longaretti P.-Y., 1994, preprint
Kochanek C. S., 1990, MNRAS, 247, 135
Koo D. C., 1981, ApJ, 251, L75
Koo D. C., Gronwall C., Bruzual G., 1993, ApJ, 415, L21
Kron R., 1978, PhD thesis, Univ. California, Berkeley
Le Fèvre O., 1993, CFHT Newsletter, No. 28
Lilly S. J., 1993, ApJ, 411, 501
Lilly S. J., Cowie L. L., Gardner J. P., 1991, ApJ, 369, 79
Mason K. O. et al., 1981, AJ, 86, 803
Metcalfe N., 1983, PhD thesis, Univ. Oxford
Metcalfe N., Fong R. F., Shanks T. S., Jones L. R., 1990, MNRAS, 249, 498
Metcalfe N., Shanks T. S., Roche N., Fong R. F., 1993, Ann. NY Acad., 688, 534
Miralda-Escudé J., 1991a, ApJ, 370, 1
Miralda-Escudé J., 1991b, ApJ, 380, 1
Oemler A., 1992, in Fabian A. C., ed., Cluster and Superclusters of Galaxies. Kluwer, Dordrecht, p. 29
Peterson B. A., Ellis R. S., Kibblewhite E. J., Bridgeland M. T., Hooley A. J., Horne D., 1979, ApJ, 233, L109
Schild R. et al., 1980, AJ, 85, 121
Smail I., Ellis R. S., Fitchett M. J., Norgaard-Nielsen H. U., Hansen L., Jorgensen H. E., 1991, MNRAS, 252, 19
Smail I., Ellis R. S., Aragón-Salamanca A., Soucail G., Mellier Y., Giraud E., 1993, MNRAS, 263, 628
Smail I., Ellis R. S., Fitchett M. J., Edge A. C., 1994, MNRAS, submitted, Paper II
Soucail G., Mellier Y., Fort B., Cailloux M., 1988, A&A, 191, L19
Spinrad H., 1980, in Abell G. O., Peebles P. J. E., eds, Proc. IAU Symp. 92, Objects of High Redshift. Reidel, Dordrecht, p. 39
Tresse L., Hammer F., Le Fèvre O., Proust D., 1993, A&A, 277, 53
Tyson A. J., 1988, AJ, 96, 1
Tyson A. J., Jarvis J. F., 1979, ApJ, 230, L153
Tyson A. J., Valdes F., Wenk R. A., 1990, ApJ, 349, L1
Valdes F., 1982, Proc. SPIE, 331, 465
White S. D. M., Frenk C. S., 1991, ApJ, 379, 52
White S. D. M., Silk J., Henry J. P., 1981, ApJ, 251, L65
Wu X. P., Hammer F., 1993, MNRAS, 262, 187
Yoshii Y., Takahara F., 1990, ApJ, 346, 28

© Royal Astronomical Society • Provided by the NASA Astrophysics Data System